

Alkaline Earth Metal Fluorides (MgF_2 , CaF_2 , SrF_2 , BaF_2) and Nb_2O_5 Effect on the Structural and Optical Properties of New Fluorophosphoniobate Glasses

Published as part of ACS Omega special issue "Chemistry in Brazil: Advancing through Open Science".

Leandro Olivetti Estevam da Silva, Lais Dantas Silva, Edgar Dutra Zanotto, Marcos de Oliveira Junior,* and Danilo Manzani*



Cite This: <https://doi.org/10.1021/acsomega.5c05892>



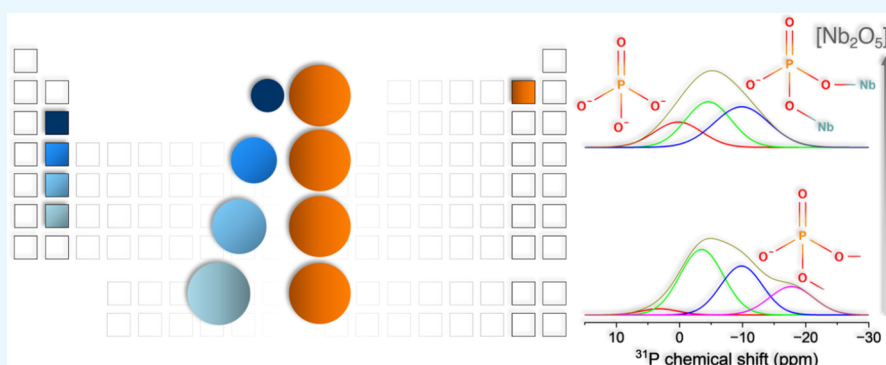
Read Online

ACCESS |

Metrics & More

Article Recommendations

Supporting Information



ABSTRACT: Niobium-fluorophosphate glasses show promising technological and scientific potential in a wide range of optical and photonic applications due to their properties as a host matrix, such as wide transparency between the ultraviolet and near-infrared, high solubility to rare-earth ions, low phonon energy, and high chemical stability. Efforts were previously made to study the effects that different concentrations of niobium oxide have on the base phosphate glass composition used here in the structural, thermal, and optical properties. However, an exploration of which changes different alkaline earth metals can induce in niobium-phosphate glass properties, considering their modifying role and periodic properties, is lacking. Therefore, this study aimed to thoroughly investigate how different alkaline earth metals can induce variations in the structural, thermal, and optical properties of a novel niobium-phosphate glass. The tested glasses followed the compositional rule $(80 - \gamma)\text{NaPO}_3 - \gamma\text{Nb}_2\text{O}_5 - 20\text{XF}_2$ ($\text{X} = \text{Mg}^{2+}$, Ca^{2+} , Sr^{2+} , Ba^{2+} , $\gamma = 5, 10, 15, 20$ mol % of Nb_2O_5) and were synthesized by the melt-quenching method. Analysis by differential scanning calorimetry (DSC), UV-vis absorption spectroscopy, and optical bandgap calculations shows that the covalent character of the glass matrix increases for increasing Nb_2O_5 content, causing an increase in the glass transition temperature, T_g , and a decrease of the optical bandgap energy. DSC analyses revealed a very high stability against crystallization, ΔT up to nearly 400 °C ($\Delta T = T_x - T_g$)—where T_x is the crystallization peak temperature—for this glass-forming system. ^{31}P NMR experiments revealed that the increase in Nb_2O_5 between 5 and 15 mol % induced the formation of P^0 , P_{INb}^1 , and P_{2Nb}^2 phosphate units, consequently increasing the glass matrix connectivity due to the formation of $\text{P}-\text{O}-\text{Nb}$ and $\text{Nb}-\text{O}-\text{Nb}$ bonds. Moreover, ^{19}F nuclear magnetic resonance showed how the alkaline earth metals with a higher charge-to-radius ratio (smaller ionic radius) preferentially bond with the fluoride species within the glass matrix. Consequently, the glass connectivity increases due to the lower availability of fluoride to interact with the main glass former groups (i.e., phosphate and niobate groups).

1. INTRODUCTION

Phosphate glasses are widely recognized for their properties of a broad transparency window spanning from UV to near-infrared, relatively low characteristic temperatures, and high solubility for rare-earth ions (RE^{3+}) when compared to silicate glasses.^{1–3} Through chemical and structural modifications, it is always possible to achieve even better properties. The addition of fluoride precursors to form fluorophosphate glasses reduces

Received: June 19, 2025

Revised: September 1, 2025

Accepted: September 16, 2025



the overall phonon energy and increases RE³⁺ solubility while preserving certain key features of oxide glasses, such as chemical stability.⁴ These properties make fluorophosphate glass matrices excellent candidates for applications in photonics.^{5,6} Due to the high volatility of fluoride compounds during the melting step at high temperatures, previous studies have focused on how synthesis conditions—such as melting temperature, time, and crucible material—influence the amount of fluorine lost and its preferential coordination with other species.⁷ In fluorophosphate glasses, fluoride induces significant alterations in the bonding environment, depending on the F/O ratio, by determining the distribution and connectivity of Qⁿ phosphate groups throughout the glass structure.⁸ Therefore, fluorination strategies for phosphate-based glass compositions must be thoroughly controlled to obtain the desired properties in the resulting fluorophosphate glass. These properties include improved transparency in the UV range and a reduced mean phonon energy of the matrix, which is highly beneficial for minimizing nonradiative decay in luminescent rare-earth-doped matrices used in photonics, such as the composition studied here.^{7–11} Previous studies have demonstrated that incorporating certain metal oxides, such as TiO₂, Nb₂O₅, and WO₃, enhances the linear and nonlinear optical properties of phosphate glasses.^{12–14} Also, adding different concentrations of Nb₂O₅ to lead pyrophosphate-based glasses significantly increases the glass transition temperature as well as the linear and nonlinear refractive indices of the resulting glass.¹³ The content of [NbO₆] units formed within the phosphate chains is highly dependent on the Nb₂O₅ content, which initially increases thermal stability against crystallization before decreasing it due to clustering.¹³ Furthermore, higher concentrations of Nb₂O₅ in phosphate glass compositions reduce hygroscopicity and enhance chemical stability.¹² These effects demonstrate promising features for the optical applications of the resulting glass, combining the advantages of fluorophosphate matrices with the Nb₂O₅ dual role as a glass former and modifier.^{4,6} Additionally, Brazil holds very large reserves of Nb, making it important to gain a deep understanding of this metal in glasses and explore new products and technologies for the national development.¹⁵

Alkali and alkaline earth metals modify the phosphate glass network in different manners by producing or stabilizing nonbridging oxygens (NBO) and lone electron pairs, thereby changing the network connectivity through electrostatic forces.¹⁶ In-depth investigations have shown that different alkali and alkaline earth metals can significantly impact the structural, thermal, optical, and spectroscopic properties of RE³⁺-doped glasses in different proportions, following a periodic trend along the group, such as in the ionic radii, electron affinity, ionization energy, and polarizability.^{17,18} Although several studies have highlighted the impact of alkaline earth metals on glass properties, this work aims to have a comprehensive understanding regarding how their periodic properties change the properties and features of the resulting glasses.^{19–21} In this sense, this systematic study focuses on the investigation of both the effects by varying the Nb₂O₅ concentration and the type of alkaline earth metal added into a sodium metaphosphate-based glass. The most important contribution is to provide knowledge of the periodic trends and their influence on the structural, optical, and thermal properties of niobium-fluorophosphate glasses.

2. EXPERIMENTAL PART

2.1. Synthesis and Characterizations of the Niobium-Fluorophosphate Glasses. Niobium-fluorophosphate glasses were synthesized by the conventional melt-quenching method according to the molar compositional rule (80 – y)NaPO₃– y Nb₂O₅–20XF₂, with X = Mg, Ca, Sr, Ba, and y = 5, 10, 15, 20 mol %, as detailed in Table 1. The glass samples

Table 1. Nominal glass composition, labels, and P/Nb ratio (X = Mg, Ca, Sr, Ba)

Sample label	Molar composition (mol %)			P/Nb ratio
	NaPO ₃	Nb ₂ O ₅	XF ₂	
Nb5-X	75	5	20	7.5
Nb10-X	70	10		3.5
Nb15-X	65	15		2.2
Nb20-X	60	20		1.5

were labeled as Nby-X. The chemicals sodium metaphosphate NaPO₃ (Aldrich, 65–70% P₂O₅ basis), magnesium fluoride MgF₂ (Aldrich, 99.9%), calcium fluoride CaF₂ (Aldrich, 99.9%), strontium fluoride SrF₂ (Aldrich, 99.9%), barium fluoride BaF₂ (Aldrich, 99.9%), and niobium oxide Nb₂O₅ (CBMM, optical grade) were thoroughly weighed, mixed, and homogenized in an agate mortar. Each powder mixture was melted in a covered Pt/Au (95/5 mol %) crucible at 1050 °C for 30 min. The melt was poured into a preheated stainless steel mold at 250–350 °C (depending on the composition) and annealed for 4 h to relieve internal stress before slowly cooling to room temperature. After annealing, the glass samples were cut, some pieces were polished for optical measurements, and other pieces were ground into powder.

The optical characterization was carried out using UV–vis–NIR spectroscopy with a Shimadzu UV-3600 spectrophotometer, scanning between 200 and 1000 nm. From the UV–vis–NIR absorption spectra, the molar absorptivity coefficients were calculated. Plots of $(\alpha h\nu)^{1/2}$, $(\alpha h\nu)^2$, and $\ln(\alpha)$ as a function of the energy $h\nu$ (in eV) were used to determine the indirect and direct bandgap energy and Urbach's energy of each sample. The thermal analysis was performed by differential scanning calorimetry (DSC) to determine the characteristic temperatures. The analysis was performed using a Netzsch STA F3 Jupiter instrument. Powdered glass samples (<20 μ m) of each composition were heated from 200 to 1000 °C in platinum crucibles under an N₂ atmosphere at a heating rate of 10 °C min^{−1}. The resulting curves were analyzed using Proteus software.

For structural characterization, Raman spectroscopy was carried out using a Jobin-Yvon Horiba HR800 instrument operating with a He/Ne laser at 632.8 nm. A detailed solid-state nuclear magnetic resonance (NMR) analysis was conducted to elucidate the effect of the cation size of four alkaline earth fluorides on the glass structure. ¹⁹F magic-angle spinning (MAS) NMR spectra were recorded in an Agilent DD2 spectrometer operating at 5.64 T (corresponding to ¹H Larmor frequency of 240 MHz), using 1.6 mm rotors spinning at 35 kHz with a DEPTH pulse sequence for background suppression,²² a 90° pulse length of 2.4 μ s, relaxation delays of 120 s, and up to 128 scans. ¹⁹F chemical shifts are reported relative to CFCl₃ using solid AlF₃ as a secondary reference (−172 ppm). Solid-state ³¹P, ²³Na, ²³Na{³¹P} REDOR, ³¹P-{²³Na} REAPDOR, and ³¹P{⁹³Nb} RESPDOR NMR experi-

ments were conducted on a Bruker Avance Neo spectrometer operating at 14.1 T (corresponding to a ^1H Larmor frequency of 600 MHz), using a 2.5 mm Bruker probe spinning at 15 kHz. The ^{31}P MAS spectra were acquired by using single-pulse excitation with a 90° pulse of 2.4 μs . A recycling delay of 300 s was used, which ensures complete recovery of the equilibrium magnetization. Up to 128 scans were accumulated for noise averaging. In a separate set of measurements, double-quantum filtered spectra were obtained using the 1-D refocused-INADEQUATE method.²³ This experiment results in the selective detection of only those ^{31}P nuclei that are involved in a P–O–P linkage (P^1 and P^2 units) and, therefore, gives rise to the excitation of double-quantum coherence through indirect ^{31}P – ^{31}P spin–spin coupling. In contrast, the signals of isolated P^0 units are suppressed by the appropriate receiver phase cycling. Experimental conditions were: spinning speed of 15 kHz, $\pi/2$ pulse length of 2.4 μs and relaxation delay of 100 s. The mixing time for DQ coherence creation was 16.6 ms, corresponding to a value of the indirect coupling constant $J(^{31}\text{P}$ – $^{31}\text{P})$ of 30 Hz. The ^{31}P chemical shifts are reported relative to a BPO_4 secondary reference (–29.3 ppm against an 85% H_3PO_4 aqueous solution). The ^{23}Na MAS spectra were obtained using single-pulse excitation with a 90° pulse of 4.57 μs , with a recycle delay of 0.5 s and accumulating up to 16 scans. $^{23}\text{Na}\{^{31}\text{P}\}$ rotational-echo double-resonance (REDOR)²⁴ measurements were acquired by using π recoupling pulses on the ^{31}P channel (pulse length of 4.572 μs) while obtaining rotor-synchronized ^{23}Na spin echoes, with a 90° pulse length of 2.286 μs , with a recycle delay of 0.5 s.

$^{31}\text{P}\{^{23}\text{Na}\}$ rotational-echo adiabatic passage double-resonance (REAPDOR)²⁵ experiments were carried out using a typical value for ^{31}P π -pulse duration of 4.9 μs , a spinning frequency of 20.0 kHz, and a recycle delay of 100 s. Dipolar recoupling was achieved by ^{23}Na pulses applied at a nutation frequency of 96 kHz (measured for solid NaF_3) and for a duration of one-third of the rotor period (16.67 μs). $^{31}\text{P}\{^{93}\text{Nb}\}$ dipolar recoupling experiments were performed using the wideband uniform rate smooth truncation–resonance rotational-echo saturation-pulse double-resonance (WURST-RE-SPDOR) pulse sequence,²⁶ where saturation of the quadrupolar spin (in the nonobserved ^{93}Nb channel) is accomplished by a frequency-swept WURST pulse.²⁷ The WURST saturation pulse parameters were optimized through SIMPSON²⁸ simulations, as reported in ref 29, and were fixed as follows: 8 rotor cycles duration (400 μs), shape parameter $N = 80$, sweep width of 450 kHz, and nutation frequency of 53.0 kHz.

^{25}Mg MAS spectra were acquired in a 3.2 mm probe using a rotor-assisted population transfer (RAPT)³⁰ approach for signal enhancement, using a rotor-synchronized Hahn-echo scheme for signal detection. Signal enhancement was provided by a wideband, uniform rate, smooth truncation (WURST) pulse²⁷ for $\text{ST} \rightarrow \text{CT}$ (satellite to central transition) population transfer, applied prior to the Hahn-echo block.^{31–33} The parameters used for the acquisition of ^{25}Mg in the present work were all optimized experimentally on an isotopically enriched $\text{CaMgSi}_2\text{O}_6$ glass sample. Magic angle spinning (MAS) was fixed at 20 kHz; for the ST inversion, we used a WURST-80 pulse with 1.0 ms of duration, 20 kHz sweep width, pulse-power corresponding to a nutation frequency of 12.5 kHz (as measured for solid MgO), and a frequency offset of 350 kHz. For the detection step, we have used $\pi/2$ and π pulses of 6.2 and 12.4 μs and an interpulse

delay of 50 μs . ^{25}Mg chemical shifts were referenced against aqueous MgCl_2 , using solid MgO as a secondary reference ($\delta = 26$ ppm).

3. RESULTS AND DISCUSSION

The glass samples were successfully obtained by using the melt-quenching method, exhibiting transparency in the visible range and absence of bubbles and fractures, as shown in Figure S1. The susceptibility of the 5 mol % Nb_2O_5 samples to atmospheric moisture varies with the alkaline earth metal. Weeks after synthesis, the Nb_5 – Ba sample underwent complete surface corrosion, resulting in total opacity. The Nb_5 – Sr and Nb_5 – Ca samples, however, showed only an initial onset of haziness (Figure S1), whereas the Nb_5 – Mg sample displayed no observable alteration. This trend was further confirmed after prolonged exposure to the environment (Figure S2), where only the Nb_5 – Mg sample maintained its transparency, with the others showing a progressive increase in surface alteration.

Recent studies, such as the one conducted by Sreenivasan et al.,³⁴ demonstrate that in quaternary sodium–magnesium aluminosilicate glass systems, the progressive increase in MgO content induces significant alterations in the glass network and promotes liquid phase separation. Using nuclear magnetic resonance of ^{29}Si and ^{27}Al , the authors observed that the substitution of Na^+ by Mg^{2+} leads to the conversion of Q^3 silicon species into Q^2 , thus reducing the polymerization of the network. Additionally, they found that due to its higher field strength, Mg^{2+} acts not only as a network modifier but also as a charge compensator, causing a redistribution of $\text{Si}^4(\text{mAl})$ species: there was a decrease in Q^4 (4Al) and Q^4 (3Al), units, along with a concomitant increase in the less coordinated Q^4 (2Al) and Q^4 (1Al) species. This structural reorganization favors the formation of silica- and alumina-rich domains, characterizing phase separation. These results reinforce the hypothesis that network-modifying cations with a higher electrostatic field strength, such as Mg^{2+} , play a decisive role in inducing and amplifying phase separation in complex systems.

Petrovskii et al.³⁵ observed that, in the Na_2O – K_2O – Nb_2O_5 – SiO_2 system, metastable liquid phase separation occurs mainly in glasses containing 15 mol % or more Nb_2O_5 , resulting in the formation of a micro inhomogeneous structure. In this structure, there are regions enriched in Nb_2O_5 and alkali, which, upon further heating, crystallize to form NaNbO_3 microcrystals.

Comparing the Nb_y – Ba samples, higher Nb_2O_5 content reduces its hygroscopicity since it acts as a glass former above certain concentrations in phosphate-based matrices.^{13,36} The presence of different alkaline earth fluorides also significantly affects the chemical stability of the obtained glasses. The cationic potential of alkaline earth metals, e.g., the ionic charge over ionic radii, was calculated for Mg^{2+} , Ca^{2+} , Sr^{2+} , and Ba^{2+} , being 2.78, 2.00, 1.72, and 1.47 \AA^{-1} , respectively.³⁷ Elements with higher cationic potential (ionic charge/radii ratio), such as Mg^{2+} , stabilize the structure against water absorption, probably due to less depolymerization of the phosphate backbone chain. In contrast, alkaline earths with lower cationic field strength, such as Sr^{2+} and, especially, Ba^{2+} , increase the phosphate-based network depolymerization and consequently increase their hygroscopicity.

Figure S3 presents the DSC thermograms obtained for all samples. The characteristic temperatures including the T_g , T_x ,

and T_g —glass transition temperature (T_g) measured at the inflection point of the endothermic peak (obtained from the first derivative of the DSC thermogram), onset crystallization temperature (T_x), and maximum crystallization temperature (T_p) obtained from the onset and peak of the exothermic event in the thermogram, respectively—were determined, and a parameter of glass stability against crystallization, ΔT , was obtained for each sample, and is listed in Table S1. Figure 1a

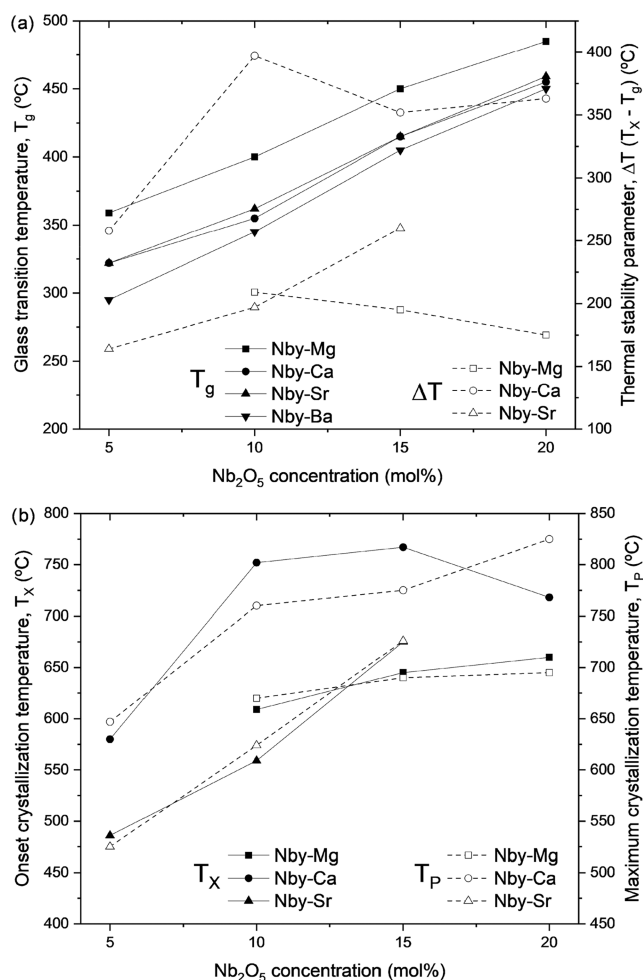


Figure 1. Behavior of (a) the glass transition temperature (T_g , solid lines) and thermal stability against devitrification (ΔT , dashed lines), and (b) the onset crystallization temperature (T_x , solid lines) and the maximum crystallization temperature (T_p , dashed lines) for all Nby-X samples. The temperatures were determined from DSC measurements.

shows the behavior of T_g as a function of the Nb₂O₅ content. The increased levels of Nb₂O₅ lead to increased T_g values, probably due to the formation of Nb–O–P and Nb–O–Nb linkages by the insertion of NbO₆ units within the phosphate backbone chain, which are stronger than the bonds of the original glass former (P–O–P).^{13,38} Cicconi et al.³⁹ demonstrated that the incorporation of Nb promotes the association of NbO₆ units, initiating the formation of a subnetwork composed of vertex-sharing NbO₆ octahedra. Similarly, Koudelka et al.⁴⁰ state that, for low Nb₂O₅ contents, niobium atoms form isolated NbO₆ octahedra. However, as the Nb₂O₅ concentration increases, these octahedra tend to cluster, leading to greater connectivity of the glass structure. It can

be clearly seen in the Raman spectra analysis. On the other hand, when the size of the alkaline earth metal increases from Mg²⁺ to Ba²⁺, maintaining the Nb₂O₅ content, the T_g values decrease by increasing their ionic radii ($r_{Ba^{2+}} > r_{Sr^{2+}} > r_{Ca^{2+}} > r_{Mg^{2+}}$). Hence, it appears that smaller ionic radii, such as those of Mg²⁺, promote a higher connectivity of the glass network and lower depolymerization compared with larger cations, thereby increasing chemical durability. The influence of alkaline earth metals' ionic radius is depicted in Figure S4, which shows the values of T_g as a function of their radius and Nb₂O₅ content.

Figure 1a depicts thermal stability against crystallization as a function of the alkaline earth and Nb₂O₅ content. Previous studies on the Pb₃P₂O₇–Nb₂O₅ system revealed that T_g increases when the P/Nb ratio decreases, while ΔT increases up to P/Nb = 2 and then decreases with lower P/Nb ratios due to the formation of NbO_n clusters. This was confirmed by Nb–O–Nb linkages that appeared in Raman spectra.^{13,41} Mošner et al. demonstrated that T_g and T_x increase when P₂O₅ is replaced by Nb₂O₅ in the Na₂O–P₂O₅–Nb₂O₅ binary glass system, while the ΔT parameter decreases.^{36,42} Stunda-Zujeva et al. studied the effect of adding CaO to the Na₂O–P₂O₅–Nb₂O₅ system. The decrease in the P/Nb ratio increased the ΔT values up to 125 °C and subsequently decreased them down to 92 °C.⁴³ Similar results were obtained for the Nb–Ca samples in this study. Increasing the Nb₂O₅ content from 5 to 10 mol % led to a significant increase in the ΔT values, from 258 to 397 °C. However, a further increase in Nb₂O₅ to 15 and 20 mol % resulted in a decrease of the ΔT values, which reached approximately 260 °C (Figure 1a). Once again, it is evident that different alkaline earth metals play a critical role in the crystallization behavior of glass compositions. Nby-Mg samples exhibited a monotonic decrease in ΔT as the Nb₂O₅ content increased from 10 to 20 mol %, while Nby-Sr samples showed a monotonic increase in ΔT from 5 to 15 mol % of Nb₂O₅, with values ranging from approximately 150 to 250 °C.

Regarding the crystallization behavior, as shown in Figure 1b, it is evident that both the onset crystallization temperature (T_x) and the maximum crystallization temperature (T_p) increase with increasing Nb₂O₅ content for all samples, except for the T_x value for the Nb20–Ca sample, which will be discussed below. The different slopes observed for a set of samples containing different alkaline earth metals highlight the critical role of these cations in the glass crystallization trends.⁴⁴ The exception observed for the Nb20–Ca sample is noticeable: T_p continues to increase relative to the Nb15–Ca sample, while T_x decreases from 767 to 718 °C. This can be interpreted as the formation of new crystalline phases at higher niobium contents. A crystallization study conducted by Stunda-Zujeva et al.⁴³ demonstrated that lower concentrations of Nb₂O₅ favored the formation of calcium phosphate-based phase formation, while higher Nb₂O₅ contents promoted the crystallization of needle-like niobate or phosphoniobate phase crystallization. Therefore, it is plausible that in the Nby-Ca glasses, the increased Nb₂O₅ content, combined with the significantly higher ΔT , led to the precipitation of new niobium-containing phases. This would explain the observed decrease in T_x without a corresponding decrease in T_p for the Nb20–Ca sample as well as why similar behavior was not observed for the Nb20–Mg and Nb20–Sr samples. These samples exhibited lower thermal stability and were thus less prone to forming niobate-based crystal phases, which require higher temperatures to precipitate.⁴³ The presence of fluorides and the influence of alkaline earth cations (Mg²⁺, Ca²⁺, Sr²⁺,

and Ba^{2+}) significantly affect the network connectivity and the crystallization tendency. Cations with smaller ionic radii, such as Mg^{2+} , promote greater structural connectivity and, consequently, higher thermal stability. In contrast, cations with larger radii, such as Ba^{2+} , tend to inhibit crystallization. This behavior demonstrates the system's remarkable ability to adjust its structure, resulting in thermal stability superior to that reported in the cited literature.⁴³

UV–vis–NIR absorption spectroscopy was performed to investigate the absorption behavior of the glasses between 200 and 1000 nm. As Figure S5 shows, all samples exhibited similar absorption profiles with high transparency from approximately 350 to 1000 nm. The electronic absorption edge shifts monotonically toward higher wavelengths as the Nb_2O_5 content increases (corresponding to a decrease in the P/Nb ratio from 7.5 to 1.5).^{13,36} This shift suggests modifications in the energy levels of the valence and conduction bands, i.e., a reduction in the optical bandgap energy (E_g), indicating that higher Nb_2O_5 concentrations enhance the covalency of the phosphate chains. This occurs through the incorporation of NbO_6 octahedra, which replace P–O–P bonds with P–O–Nb and Nb–O–Nb bonds. The increase in covalency also correlates with an increase in the optical basicity of the glass network because the higher Nb_2O_5 content increases the number of nonbridging oxygens, primarily by altering the phosphate backbone chains.⁴⁵ Across the different compositions, the same absorption behavior was observed regardless of the alkaline earth metal, except for the Nb–Ba samples. Figure 2 illustrates the shift in the absorption edge for the Nb20-X

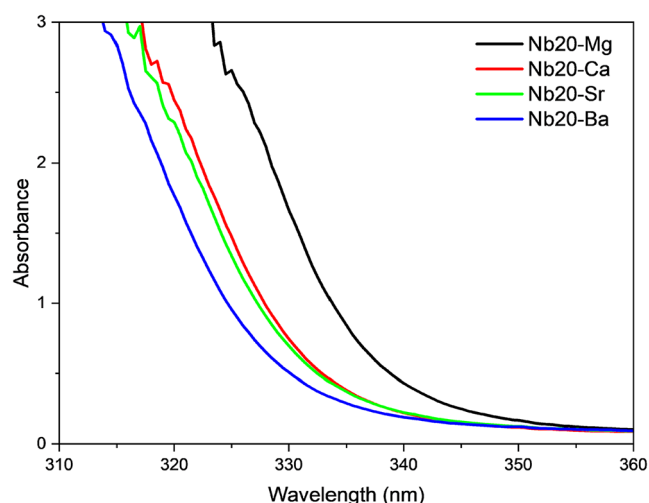


Figure 2. Absorption edge in the UV range for all Nb20-X samples, showing the shift based on different alkaline earth metals.

samples. This shift is associated with a decrease in the ionic character of the glass network as the ionic radius of the alkaline earth metal decreases, accompanied by a tendency to lose valence electrons. This observation is consistent with the previously discussed trend in glass transition temperatures, where T_g decreases as the ionic radius of the alkaline earth cation increases.

The optical bandgap value was calculated from the UV–vis–NIR absorption data. Optical transitions occur directly or indirectly between the valence and conduction bands within the optical bandgap. The optical bandgap relates to the molar absorptivity coefficient through the following equation:^{46,47}

$$\alpha h\nu = B(h\nu - E_g)^s \quad (1)$$

in which s alternates between 1/2 for direct optical transitions and 2, for indirect transitions, h represents Planck's constant, ν is the frequency, B is an energy-independent constant, E_g is the energy of the optical bandgap, and α is the linear absorption coefficient, calculated from the relation $\alpha = 2.303 \times \frac{A}{d}$, where A is the absorbance and d is the thickness of the glass.^{47,48} The Urbach energy, related to the width of the band tail within conduction and valence bands, can be calculated by the equation:⁴⁶

$$\alpha(\nu) = \alpha_0 \exp\left(\frac{h\nu}{\Delta E}\right) \quad (2)$$

or by plotting $\ln(\alpha)$ against $h\nu$, and its values and trends are frequently associated with the degree of defects within a disordered material.⁴⁹ Figure S6 shows the graphic method used to obtain Urbach energy (E_U) and the direct and indirect optical bandgap ($E_{\text{dir.}}$ and $E_{\text{indir.}}$) values, by plotting $\ln(\alpha)$, $(\alpha h\nu)^2$, and $(\alpha h\nu)^{1/2}$, respectively, as a function of the photon energy, $h\nu$ (eV). Extrapolating the linear portion of these curves (the region correlated with the absorption edge of the samples) provides the approximate values for the optical bandgap, shown in Figure 3. With the increase in Nb_2O_5 content (decrease in the P/Nb ratio), a higher covalency of the glass network is expected due to the NbO_6 octahedra insertion, which strongly interacts within the phosphate units, increasing the number of NBO.^{13,47} This change is responsible for the observed red shift of the absorption edge in the samples, leading to a reduction in both the direct and indirect optical bandgap values, as shown in Figure 3a. Along with the decrease in $E_{\text{dir.}}$ and $E_{\text{indir.}}$, with increasing Nb_2O_5 molar concentration, the ΔE value also decreases from an average of 0.22 eV in Nb5-X samples to ~0.17 eV in Nb20-X samples, as shown by the bars in Figure 3a. Figure 3b shows that increasing Nb_2O_5 concentration results in a decrease in the E_U , suggesting that lower P/Nb ratios lead to a less disordered structure due to the formation of NbO_6 ordered clusters.⁴⁹ These trends were consistently observed in all synthesized samples, regardless of the alkaline earth metal. The Nb5–Ba sample, however, is not shown due to its anomalous behavior in the absorption spectra.

Unlike the clear monotonic shift in E_g values observed with varying Nb_2O_5 content, changes in the alkaline earth metal led to more complex behavior, as shown in Figure 3. Alkaline earth metals are known to be glass modifiers, acting as stabilizing nonbridging oxygens (NBOs) and linking phosphate–niobate chains through electrostatic interactions.¹⁶ Unlike Nb_2O_5 , which can act as a network modifier or former depending on its concentration, variations in the alkaline earth metals provoke less pronounced shifts in the absorption edge, as well as in the E_g and E_U values, compared to the changes induced by variations in the P/Nb ratio. Several studies have correlated changes in various glass properties with their cationic potential (Z/r ratio).^{19,50} In this context, the variations observed in Figure 3, in which the Mg-containing samples exhibit significantly lower $E_{\text{indir.}}$, $E_{\text{dir.}}$, and E_U values, can be attributed to Mg^{2+} higher cationic potential compared with the other alkaline earth metals. Differences in optical bandgap values among the various alkaline earth metals become more pronounced with increasing Nb_2O_5 content. This suggests an enhancement of the covalent character of the mean glass linkages resulting from a decrease in alkaline earth metal ionic

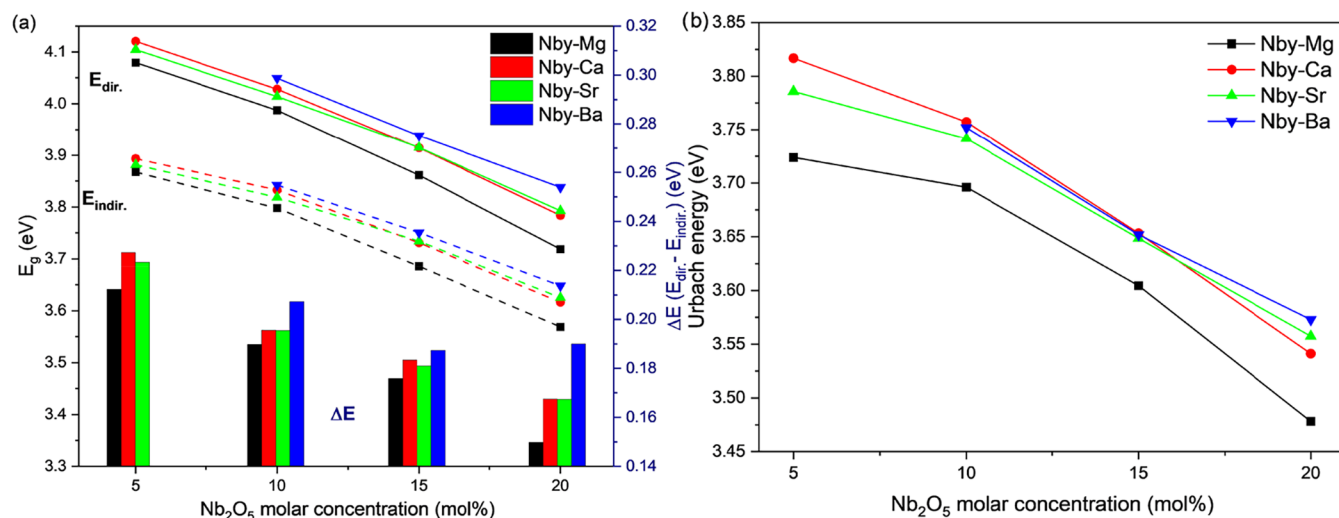


Figure 3. Direct and indirect optical bandgap energy values (E_{dir} and E_{indir}), represented as solid and dashed lines (respectively) and symbols, and ΔE ($E_{dir} - E_{indir}$), represented as bars (a), and Urbach energy calculated for all Nby-X glass samples (b).

radius (or an increase in electronegativity/cationic potential), which increases in the presence of higher Nb_2O_5 concentrations. This behavior implies that the substitution of different alkaline earth metals primarily affects the niobate $[NbO_6]$ units incorporated into the phosphate backbone chains while exerting a comparatively smaller influence on the phosphate network itself. Supporting this conclusion, ^{25}Mg NMR results indicate that the local coordination environment of the alkaline earth metal is strongly affected by the presence of $[NbO_6]$ units, as will be discussed later. Furthermore, for the Nb20-X samples, the optical bandgap values show a clear correlation with the electronegativity of the alkaline earth metals, exhibiting a decrease in E_g with increasing electronegativity, which varies as 0.89, 0.95, 1.00, and 1.31 for Ba^{2+} , Sr^{2+} , Ca^{2+} , and Mg^{2+} , respectively, according to Pauling's electronegativity scale.⁵¹

Regarding the E_U values (Figure 3b), while the samples containing Ca^{2+} , Sr^{2+} , and Ba^{2+} display similar values with only minor variations, the Mg^{2+} -containing glasses exhibit different behavior. The consistently lower E_U values observed for the Nby-Mg glasses, regardless of Nb_2O_5 content, suggest a significantly lower degree of structural disorder. This behavior is attributed to the smaller ionic radius and higher cationic potential of Mg^{2+} compared to the other alkaline earth metals, which contribute to a decrease in their thermal stability against devitrification.

Raman spectroscopy was used to investigate the effect of varying Nb_2O_5 content and different alkaline earth metals on the structural role of the niobium-fluorophosphate glass network. As shown in Figure S7, spectra are grouped according to the alkaline earth metal used, and the individual curves within each group correspond to different Nb_2O_5 concentrations. As expected, variation in the P/Nb ratio significantly influenced the Raman spectra, primarily due to the intermediate role of Nb_2O_5 acting as both a network modifier and a former. This dual behavior enables Nb_2O_5 to directly modify the phosphate network by inserting NbO_6 octahedra and promoting the formation of P–O–Nb and Nb–O–Nb linkages. Progressive increases in the Nb_2O_5 content result in noticeable changes in the spectrum, reflecting these structural modifications. While the most significant spectral changes are related to the Nb_2O_5 concentration, variations in the alkaline

earth metal also led to noticeable structural modifications, as discussed further.

Figure 4 illustrates the changes in the Raman spectral features as a function of increasing the Nb_2O_5 concentration, using the Mg^{2+} -containing sample set as a representative example. All characteristic bands observed in this spectrum are present in the other compositions, with differences primarily in

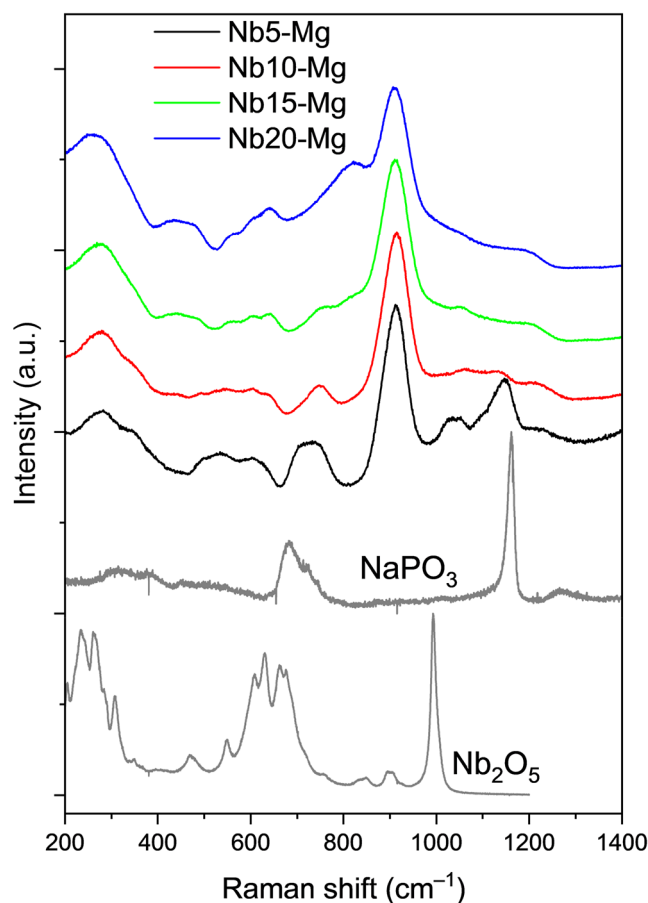


Figure 4. Raman spectra of the samples Nby-Mg ($y = 5, 10, 15$, and 20 mol % of Nb_2O_5) and the precursors Nb_2O_5 and $NaPO_3$.

the intensity and slight shifts in the position of the bands, addressed in the forward discussions. As previously discussed, the incorporation of NbO_6 octahedra at higher Nb_2O_5 contents significantly alters the phosphate glass network. The vibrational mode assignments corresponding to each spectral feature are summarized in Table 2, using the notation P^n to

Table 2. Main bands seen on the Raman spectra of $\text{Nb}_y\text{-X}$ samples (approximate values in cm^{-1} as same bands show different positions as a function of X and y) and attribution to molecular modes

Wavenumber (cm^{-1})	Assigned mode	References
276	O–P–O + O–Nb–O coupled deformation mode	13,52,53
430	O–P–O + O–Nb–O coupled mode	13,52,53
641	Nb–O vibrations	13,52–54
754	P–O–P symmetric bonding	13,52,53
824	Nb–O–Nb deformation mode	13,52–54
912	Nb–O short bond in NbO_6	13,52,53
1024	P^0 (PO_4^{3-}) symmetric stretching vibration	13,52,53
1047	P^1 (OPO_3^{2-}) symmetric stretching vibration	13,52,53
1150	P–O–P symmetric vibration	13,52,54
1216	P^2 P–O–P stretching vibration	47,48

represent phosphate units with n bridging oxygens.^{13,36,52} The principal Raman bands, apart from the one at 910 cm^{-1} , are located at 1024, 1047, 1150, and 1216 cm^{-1} , and are attributed to the symmetric stretching of P^0 units (PO_4^{3-}), symmetric stretching of P^1 units (OPO_3^{2-}), symmetric stretching of P–O–P, and the stretching vibration of P–O–P in P^2 units, respectively. A consistent decrease in the intensity of these bands with increasing Nb_2O_5 content indicates a progressive disruption of the phosphate network, particularly in involving the P–O–P bridges. This structural alteration is attributed to the formation of P–O–Nb bonds as NbO_6 units are integrated into the glass network, a phenomenon further corroborated by the ^{31}P nuclear magnetic resonance results.

Although P–F bonds can be weakly detected in fluorophosphate glass around 700 and 860 cm^{-1} , as previously reported by Möncke and Eckert, these possible bands are overlapped by the broad and highly intense niobate bands, particularly the one centered at 824 cm^{-1} .⁴ A similar effect was previously reported by da Silva et al. in lead pyrophosphate glasses with compositions $\text{Pb}_2\text{P}_2\text{O}_7\text{-Nb}_2\text{O}_5\text{-XF}_2$ (where $X = \text{Mg, Ca, Sr, and Ba}$),⁵⁵ in which P–F bonds were also undetectable by Raman spectroscopy. To reliably assign these bonds, ^{19}F NMR measurements were performed, and the results are presented on the following pages.

As the concentration of Nb_2O_5 increases, the intensity of the bands located at 276 , 430 , 641 , and 824 cm^{-1} —which are attributed to Nb–O bonds in different distorted NbO_6 octahedra—increases as well.^{13,48} As previously reported, the H– Nb_2O_5 polymorph is the most stable form under the high-temperature conditions employed during glass synthesis (above $1000\text{ }^\circ\text{C}$).¹³ The Nb–O–Nb bending mode at $\sim 250\text{ cm}^{-1}$ is indicative of the clustering of NbO_n units within the phosphate network.¹³ The increasing intensity of these low-frequency bands with a higher Nb_2O_5 content suggests the formation of niobate-rich domains, which is relevant to understanding the crystallization behavior. These results confirm that higher Nb_2O_5 concentrations promote substantial structural reorganization of the glass network's structure, primarily by disrupting the phosphate backbone and forming new Nb–O linkages. Furthermore, the substitution of different alkaline earth metals also induces significant structural variations, as evidenced by changes in the Raman spectra.

Figure 5 presents the differences in the Raman spectral band profiles for glasses containing 5 and 20 mol % of Nb_2O_5 with different alkaline earth modifiers. The most prominent change observed in the Raman spectra bands is the systematic shift of vibrational bands to lower wavenumber values with an increasing ionic radius of the alkaline earth metal. In Figure 5a, the main band at approximately 900 cm^{-1} progressively shifts from 912 to 900 cm^{-1} when the alkaline earth metal periodically changes from Mg^{2+} to Ba^{2+} . A similar trend is evident in Figure 5b, where the band shifts from 907 to 894 cm^{-1} across the same series, averaging a downshift of

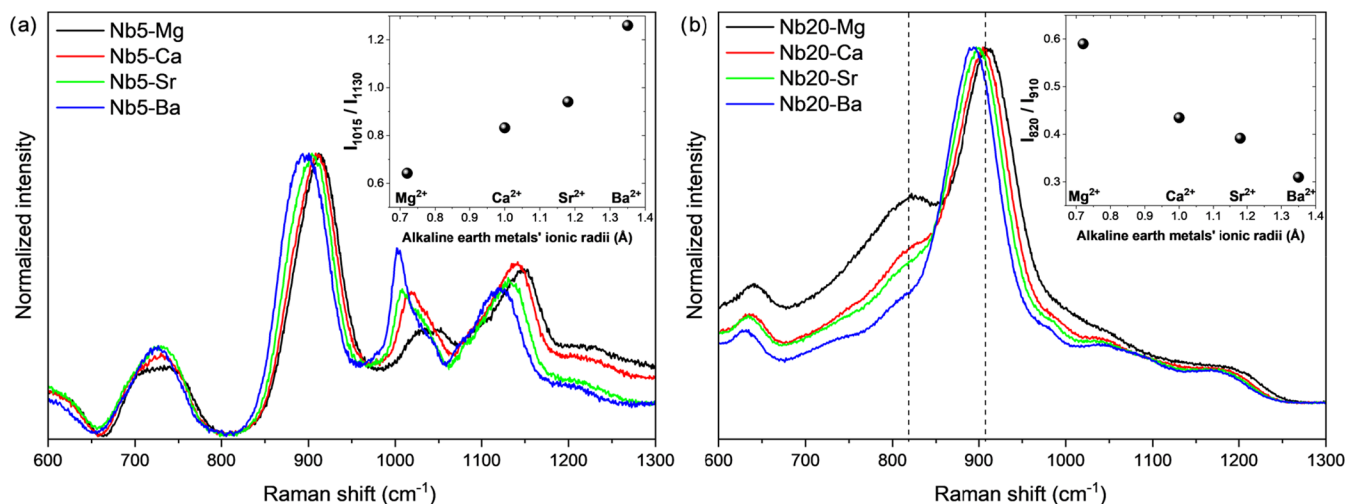


Figure 5. Raman spectrum of glass samples (a) $\text{Nb}_5\text{-X}$ and (b) $\text{Nb}_{20}\text{-X}$ in a shorter Raman shift range (cm^{-1}), demonstrating the most noticeable differences caused in the spectra due to the different alkaline earth metals contained in the samples. Inset figures exhibit (a) the intensity ratios of the bands at $\sim 1015\text{ cm}^{-1}$ by the bands at $\sim 1130\text{ cm}^{-1}$ (I_{1015}/I_{1130}) and (b) the intensity ratios of the bands at $\sim 820\text{ cm}^{-1}$ by the bands at $\sim 910\text{ cm}^{-1}$.

approximately 4 cm^{-1} per metal. This red shift reflects a periodic structural response induced by the incorporation of increasingly larger cations into the glass matrix. As reported in the literature, alkaline earth metals occupy positions between the niobium-phosphate chains within the glass network and exert electrostatic interactions with nonbridging oxygens.¹⁶ The observed shift in the Raman bands is attributed to the elongation of P–O and Nb–O bonds, likely caused by the accommodation of larger cations, which perturb the local bonding polarizability environment.⁵² This effect also correlates with the decrease in T_g as the ionic radius of the alkaline earth metal increases.

In addition to the wavenumber shifts, variations in the relative intensities of specific Raman bands are also evident. As shown in Figure 5a, notable changes are observed in the bands centered around 1015 and 1130 cm^{-1} , assigned to symmetric stretching vibrations of P^0 and P^1 phosphate units, respectively. The increase in the relative intensity of the P^0 compared to the P^1 band, as shown in the inset ratio I_{1015}/I_{1130} , suggests that larger alkaline earth cations promote the formation of more isolated phosphate tetrahedra. This indicates a higher degree of depolymerization within the phosphate network. These findings are consistent with observations from DSC and ^{31}P MAS NMR measurements and suggest that the incorporation of larger alkaline earth metals results in a less connected glass structure.

Figure 5b shows that the higher niobium content in the Nb20-X glass samples reduces the prominence of phosphate-related Raman bands, particularly those above 1000 cm^{-1} . This is primarily due to the strong polarizability of niobium-containing structural units. Nevertheless, a clear trend is evident in the relative intensities of bands at ~ 820 and $\sim 910\text{ cm}^{-1}$. The band at $\sim 820\text{ cm}^{-1}$, attributed to the asymmetric deformation of Nb–O–Nb linkages in edge-sharing NbO_6 octahedra forming chain-like structures, decreases in intensity relative to the band at $\sim 910\text{ cm}^{-1}$, which corresponds to the symmetric stretching of Nb–O bonds in isolated NbO_6 units.^{52,54} The I_{820}/I_{910} ratio is depicted in the inset of Figure 5b. This behavior suggests that alkaline earth metals with higher cationic potential and smaller ionic radii (e.g., Mg^{2+}) favor the clustering of NbO_6 units and promote the formation of niobate chains. In contrast, cations with a lower cationic potential (e.g., Ba^{2+}) tend to stabilize more isolated NbO_6 units. The observed variations in the $820/910\text{ cm}^{-1}$ intensity ratio reflect the modifying effect of the alkaline earth metal on the glass structure by modulating the organization of both phosphate and niobate units according to periodic trends in charge/radius ratio and electronegativity.

For the sake of clarity, the notation P_m^n will be adopted in this section to describe phosphate structural units, where n denotes the total number of bridging oxygens (BOs) and m represents the number of P–O–Nb linkages. This classification provides a more precise description than the conventional Q^n notation when discussing heteroatomic environments involving Nb–O–P bonds. Figure S8 shows the ^{31}P MAS NMR spectra for all sample sets. Resonances for the Nby–X glasses appear within the range of approximately 0 to -30 ppm . While the spectra are remarkably similar across different alkaline earth metals, more pronounced changes are observed with an increasing Nb_2O_5 content. For glasses containing 5 mol % Nb_2O_5 , the spectra exhibit a dominant resonance at -8 ppm , accompanied by a less intense signal near -20 ppm . As the Nb_2O_5 concentration increases to 10,

15, and 20 mol %, the -20 ppm peak progressively decreases and eventually vanishes. Meanwhile, the broader signal around -8 ppm shifts toward higher chemical shift values.

To enhance the spectral resolution and better elucidate the magnetic environments of phosphorus nuclei, additional ^{31}P NMR measurements were performed using different pulse sequences. While Figure S8 illustrates the patterns obtained using the single-pulse sequence, Figure 6 compares spectra

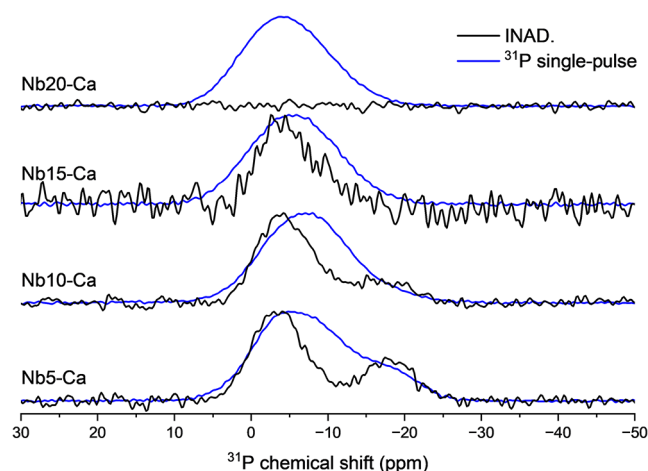


Figure 6. Nuclear magnetic resonance spectrum of the Nby-Ca sample set ($y = 5, 10, 15$, and 20 mol % of Nb_2O_5), monitoring the ^{31}P , with experimental data from the single-pulse and refocused INADEQUATE spin-echo (INAD) experiments.

from the Nby-Ca sample set obtained using both single-pulse and refocused INADEQUATE (INAD) techniques.²³ The INAD sequence, which relies on the excitation and detection of double-quantum coherence, enables the selective observation of ^{31}P species engaged in homonuclear dipolar couplings, particularly those involved in P–O–P linkages. The whole Nby-Ca sample set is shown to demonstrate how different Nb_2O_5 concentrations influence the ^{31}P NMR spectra. Also, samples Nb5–Mg and Nb20–Mg were measured (as shown in Figure S9a) comparing the single-pulse and INAD experiments) to demonstrate the high similarity between samples containing different alkaline earth metals, showing that the prominent effect is caused by the Nb_2O_5 in this case and not the different modifier metal contained in the glass.

After acquiring the single-pulse and INAD ^{31}P NMR spectra, deconvolutions of the single-pulse spectra were carried out using the chemical shift positions and line widths obtained from the INAD spectra as fixed parameters. This approach enables the deconvolution of the missing bands by comparing the INAD peaks to the total spectrum obtained by one pulse, facilitating the identification of each distinct resonance peak. The deconvolution of the spectrum is shown in Figure 7 for the Nby-Ca samples containing 5, 10, 15, and 20 mol % of Nb_2O_5 , while the deconvolution of Nb5–Mg is shown in Figure S9b. The spectra related to the sample Nb20–Ca were not deconvoluted in the same way due to the nondetectable signal with the INAD experiment. Raman spectroscopy reveals that P–O–P linkages are present for this sample (between 1500 and 1220 cm^{-1}), and Figure S10 depicts the high similarity between samples Nb15–Ca and Nb20–Ca, mainly above 950 cm^{-1} (phosphate groups, as assigned in Table 2). Hence, the lack of signal in the INAD experiment is probably

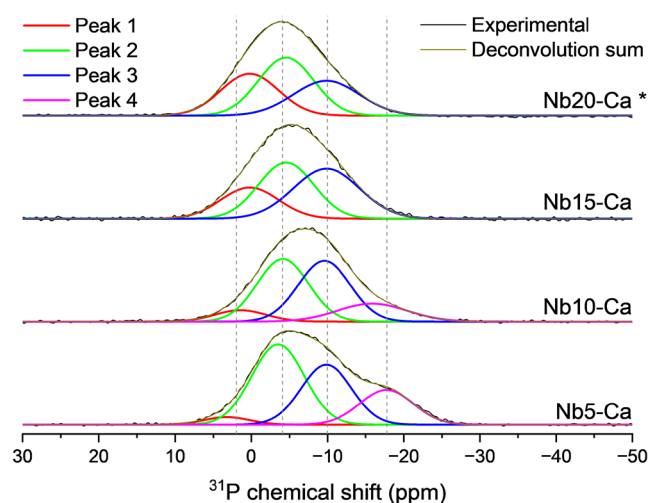


Figure 7. Nuclear magnetic resonance spectrum of the Nby-Ca series of samples ($y = 5, 10, 15$, and 20 mol % of Nb_2O_5), monitoring the ^{31}P nucleus, with deconvolution of the bands from the refocused-INADEQUATE spin-echo (INAD) experiment, with rotation at 15 kHz. Nb20-Ca is marked with an asterisk (*) due to the nonappearance of the INAD signal. Deconvolution was based on Nb15-Ca's peak position and width.

caused by very short spin-spin transversal relaxation times due to strong dipolar interactions with ^{93}Nb . Therefore, information about P-O-P connectivity is not definitive from solid-state NMR alone. Hence, the deconvolution for Nb20-Ca was performed by using the same parameters (peak location and width, in parts per million) as used for Nb15-Ca, and the relative areas were tentatively calculated (marked with an asterisk in Table 3).

As indicated by the dashed lines over the spectra in Figure 7, by using this double-quantum filtering technique approach, we could identify four spectral components at approximately -17 , -10 , -4 , and 2 ppm. Table 3 shows the areas corresponding to each peak observed from the deconvolution of the ^{31}P NMR spectra, the variations in the peak center, and the assigned phosphate groups (Figure 7), while Table S2 shows these variables related to the deconvolution of Nb5-Mg glass (Figure S9b). The components at -17 and -4 ppm are present in the INAD spectra, indicating that they are assigned to phosphate groups containing P-O-P bonds. In contrast, the components located at -10 and 2 ppm are absent in the INAD spectra, indicating that they do not participate in P-O-P linkages. Therefore, these components can be assigned to only one of the following species: P^0 , P_{INb}^1 , or $\text{P}_{2\text{Nb}}^2$ ($\text{P}_{3\text{Nb}}^3$ is ruled out by Raman data). Considering the chemical shift information,⁵⁶ compositional variations, and $^{31}\text{P}\{^{93}\text{Nb}\}$ RESPDOR data described below, we attribute the resonance at 2

ppm to mixed contributions from P^0 and P_{INb}^1 units and the component in -10 ppm to P_{ONb}^1 units. On the other hand, also based on the literature and on RESPDOR data, assignments can be found for the resonances at -17 and -4 ppm.⁵⁶ The line at -17 ppm can be attributed to a mixture of P_{ONb}^2 and P_{INb}^2 ($\text{P}_{0/\text{INb}}^2$), with an increasing contribution of P_{INb}^2 , as indicated by the broadening and low-field shift of this line (RESPDOR data show that this low-field shift is expected for higher m values in $\text{P}_{m\text{Nb}}^n$ units). Finally, the component at -4 ppm is attributed to the P_{ONb}^1 species.

With increasing Nb_2O_5 concentration, there is a clear decrease of the ^{31}P resonance corresponding to $\text{P}_{0/\text{INb}}^2$, with the complete disappearance of this peak in 15% Nb_2O_5 . The decrease in this component is followed by a decrease in P_{ONb}^1 (-4 ppm) and an increase in the concentration of $\text{P}_{2\text{Nb}}^2$ (-10 ppm) and P_{INb}^1 and P^0 species (2 ppm). This behavior underscores the formation of P-O-Nb and Nb-O-Nb bonds to the detriment of the P-O-P bond.^{57,58} These alterations, also discussed using DSC and Raman spectroscopy techniques, are reiterated by the NMR results.^{52,54,59} Also, similar behavior regarding the progressive alteration of the phosphate groups by decreasing the P/Nb molar ratio was previously reported for glasses based only on Na_2O , P_2O_5 , and Nb_2O_5 .^{36,54}

Figure 8 presents the overlaid ^{31}P NMR spectra to illustrate how the resonance peaks shift with the incorporation of different alkaline earth metals into the glass matrix. While the overall spectral pattern remains consistent across samples containing different alkaline earth metals, it undergoes significant changes with varying Nb_2O_5 concentrations. A closer comparison of spectra for samples with the same Nb_2O_5 content but different alkaline earth metals (Figure 8a) reveals a progressive high-field shift of the main resonance peak, which correlates with the cationic potential (Z/r) of the modifying cation ($2.78, 2.00, 1.72$, and 1.36 \AA^{-1} for Mg^{2+} , Ca^{2+} , Sr^{2+} , and Ba^{2+} , respectively). Alkaline earth metals with smaller ionic radii, such as Mg^{2+} and Ca^{2+} , exhibit higher cationic potentials, resulting in a more pronounced shift of the ^{31}P NMR resonance peaks toward lower chemical shift values (higher shielding). This effect is attributed to the periodical increase in the covalent character of the interaction between the alkaline earth cations and the NBOs from Ba^{2+} to Mg^{2+} , which enhances the electronic shielding of the phosphorus nuclei bonded to these NBOs.^{56,57,60}

The ^{23}Na NMR spectra for all 16 Nby-X glass samples are shown in Figure S11. All spectra display a single broad resonance centered at around -14 ppm, corresponding to sodium ions in a disordered glassy environment. Notably, a sharp signal at -5.4 ppm is observed in the spectra of the Ca^{2+} , Sr^{2+} , and Ba^{2+} samples with 5 mol % of Nb_2O_5 , indicating the presence of a partially crystallized phase. This effect is not

Table 3. Assigned phosphate groups and relative areas related to each peak (in %) from the deconvolutions of Nby-Ca samples ($y = 5, 10, 15$, and 20 mol % of Nb_2O_5), in Figure 7

Assigned phosphate groups	Chemical shift (ppm)	Relative area (%)			
		Nb5-Ca	Nb10-Ca	Nb15-Ca	Nb20-Ca ^a
$\text{P}^0 + \text{P}_{\text{INb}}^1$	0.2 to 3.2	3	7	22	30
P^1	-3.5 to -4.5	45	39	38	40
$\text{P}_{2\text{Nb}}^2$	-9.7 to -9.8	32	39	40	30
$\text{P}_{\text{INb}}^2 + \text{P}_{\text{ONb}}^2$	-15.9 to -17.7	20	15	0	0

^aNb20-Ca relative areas were tentatively calculated based on the deconvolution with the same peak parameters as Nb15-Ca.

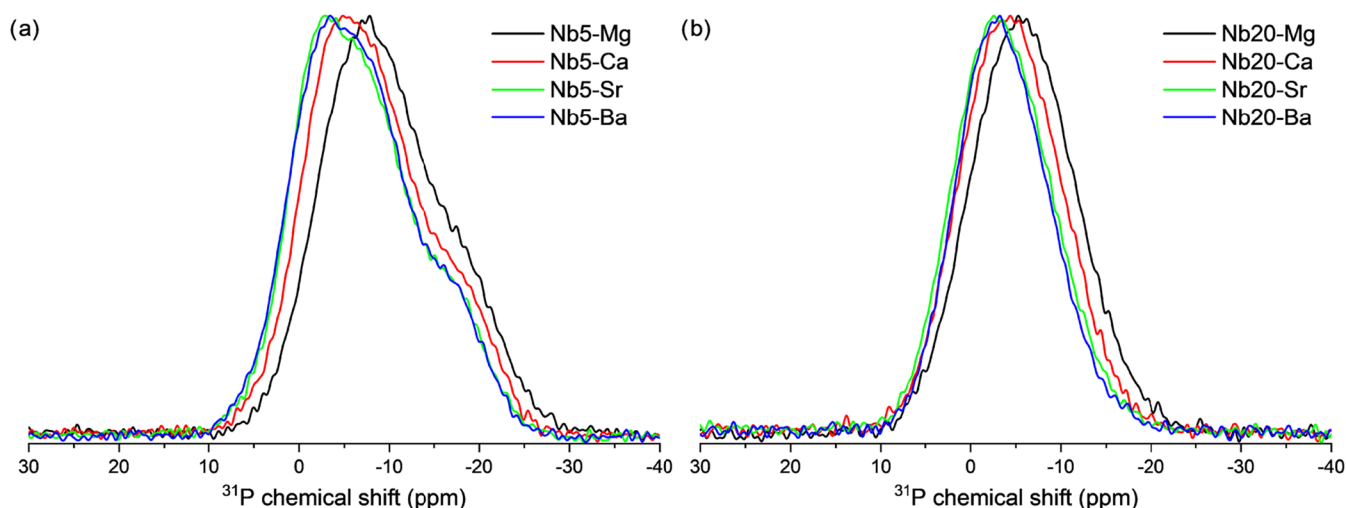


Figure 8. Spectra of nuclear magnetic resonance curves, monitoring the ^{31}P of samples (a) Nb5-X and (b) Nb20-X, rotated at 15 kHz.

observed in the Mg-containing glass, suggesting that partial crystallization is dependent on the nature of the alkaline earth metal. The low Nb_2O_5 content increases the hygroscopicity of the glasses, making them more prone to absorbing atmospheric moisture.⁶¹ This behavior is consistent with the loss of transparency observed in bulk samples containing 5 mol % of Nb_2O_5 , except for the Nb5–Mg glass, which maintained its transparency since synthesis—corroborating the findings from the ^{23}Na NMR results.

Direct comparisons of the ^{23}Na spectra are shown in Figure S12, as a function of Nb_2O_5 concentration for the Nby-Mg system (Figure S12a), and as a function of alkaline earth metal species samples containing 20 mol % of Nb_2O_5 (Figure S12b). Only minor, though systematic, chemical shift variations are observed, indicating that the alkaline earth cations and Nb-containing units primarily influence the second coordination sphere of the Na^+ environment. This interpretation is supported by the $^{23}\text{Na}\{^{31}\text{P}\}$ REDOR^{62,63} results, shown in Figure S13 of the Supporting Information, which demonstrate that the ^{23}Na – ^{31}P coordination environment remains largely consistent across all samples.

$^{31}\text{P}\{^{23}\text{Na}\}$ REAPDOR experiments were also obtained only for the Nby-Mg glass series, and the resulting dephasing curves are shown in Figure 9 in comparison to the reference curve for the $\text{Na}_2\text{PO}_3\text{F}$ crystal. Similar to the $^{23}\text{Na}\{^{31}\text{P}\}$ REDOR experiments, these results show that even when altering the Nby-Mg glasses from 5 to 20 mol % of Nb_2O_5 , the difference in the dephasing between phosphorus and sodium nuclei is not significant, showing a similar behavior of $\Delta S/S_0$ in function of the time. Also, Table S3 depicts the calculated values for experimental second moments ($M_{2(\text{Na-P})}^{\text{exp.}}$) and the calculated number of phosphorus (N_{P}), demonstrating similar behavior for the whole Nby-X glass sets. This confirms that the phosphorus environment is also not changing, in terms of the amount and proximity of sodium species, when altering the Nb_2O_5 molar concentration. To further analyze how the ^{31}P and ^{23}Na interaction induces changes onto the ^{31}P NMR spectra, Figure 10 compares the S_0 , S , and ΔS for samples Nb5–Mg (Figure 10a,b) and Nb20–Mg (Figure 10c,d) at different times of evolution, being 0.5 ms (Figure 10a,c) and 0.8 ms (Figure 10b,d).

The comparison presented in Figure 10 demonstrates that the ^{31}P nuclei resonating near -4 ppm are interacting most

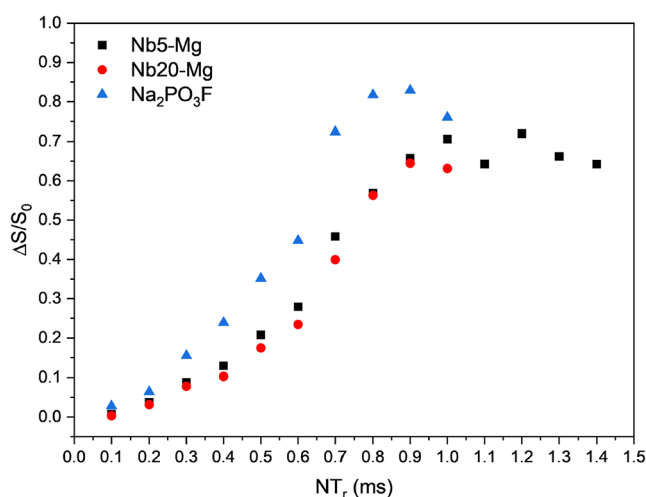


Figure 9. $^{31}\text{P}\{^{23}\text{Na}\}$ REAPDOR dephasing curves obtained for Nb5–Mg and Nb20–Mg glass samples, along with the reference measured for the $\text{Na}_2\text{PO}_3\text{F}$ crystal.

strongly with the ^{23}Na nuclei. The shape of the ΔS curve remains consistent across different samples for a given evolution time and also when comparing the same sample at different evolution times. The consistency with the REAPDOR effect suggests that no considerable differentiation in the Na–P interactions occurs with the explored variables in the studied glass compositions. As expected, increasing the evolution time from 0.5 to 0.8 ms leads to a higher ΔS intensity, reflecting an increased dipolar coupling between the ^{31}P and ^{23}Na nuclei. However, the similar intensity changes observed across samples further support the conclusion that variations in the Nb_2O_5 content do not substantially affect the coordination environment between sodium and phosphorus.

$^{31}\text{P}\{^{93}\text{Nb}\}$ RESPDOR experiments were conducted mainly to visualize how the recoupling of the ^{93}Nb dipolar interaction would suppress the ^{31}P magnetic resonance, depending on the time (amount of rotor cycles) and on the Nb_2O_5 concentration in the glass. Figure 11 depicts the $\Delta S/S_0$ dephasing as a function of time, for up to 16 rotor cycles (400 μs), for samples Nb10–Mg and Nb20–Mg. Qualitative information can be obtained from these curves. The RESPDOR dephasing is more pronounced for the sample containing a higher concentration

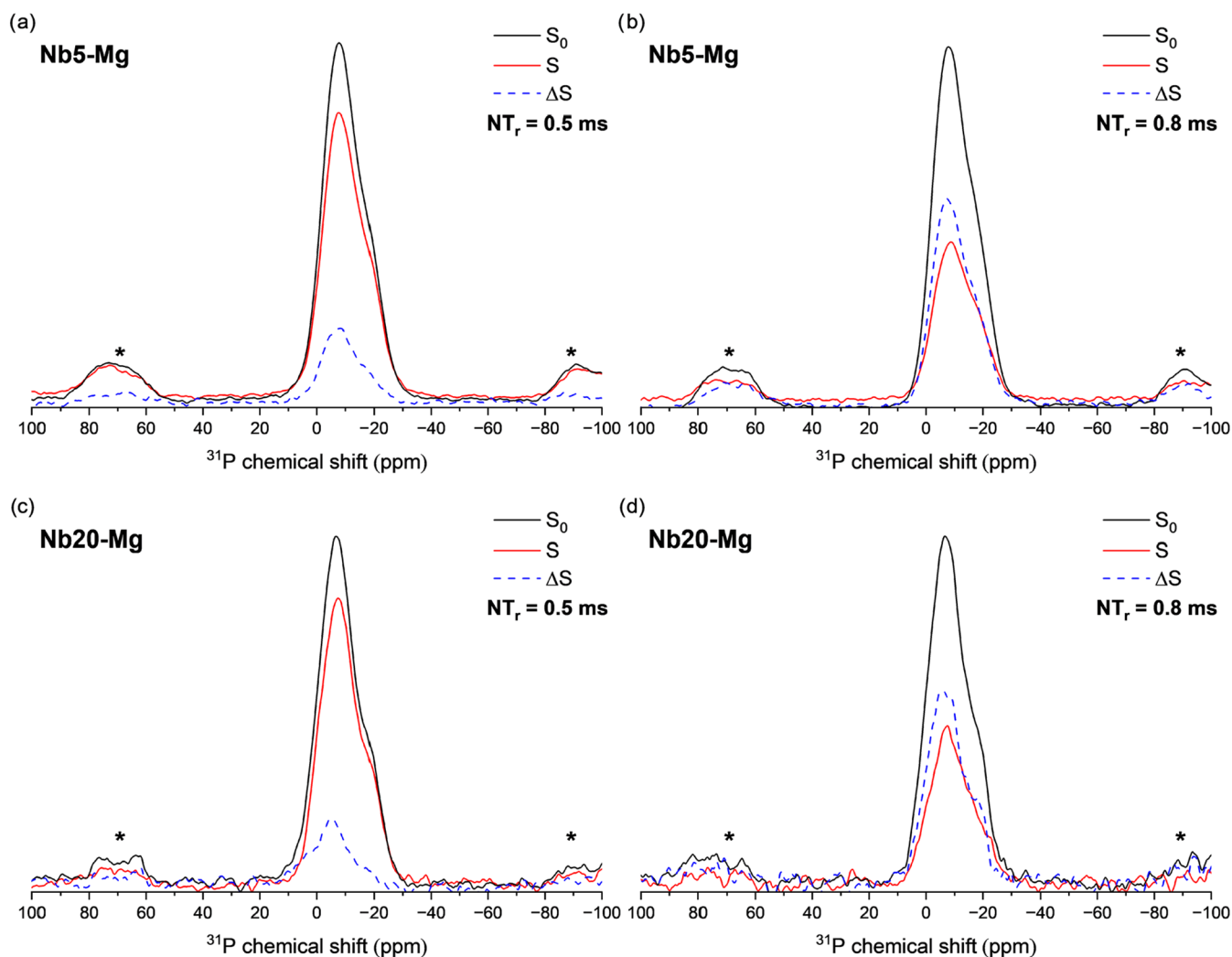


Figure 10. $^{31}\text{P}\{^{23}\text{Na}\}$ REAPDOR results obtained for Nb5–Mg (a, b) and Nb20–Mg (c, d) glass samples, depicting the S_0 (black curve), S (red curve) and $\Delta S = S_0 - S$ (dashed blue curve) for ten rotor cycles ($500\ \mu\text{s}$) (a, c) and 16 rotor cycles ($800\ \mu\text{s}$) (b, d).

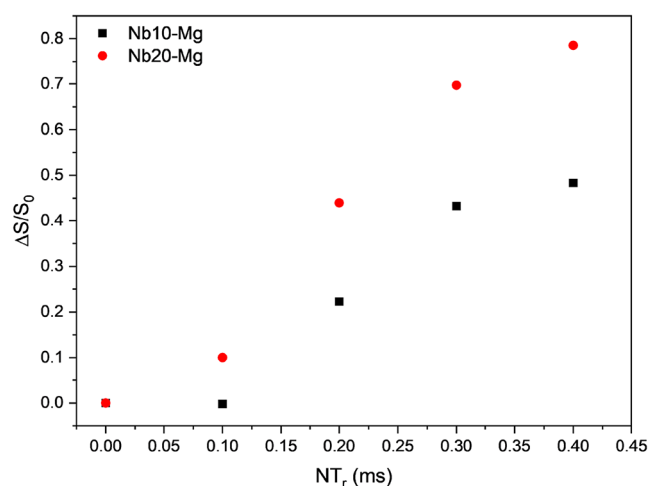


Figure 11. $^{31}\text{P}\{^{93}\text{Nb}\}$ RESPDOR dephasing curves obtained for the Nb10–Mg and Nb20–Mg glass samples.

of Nb, confirming our previous attributions regarding the formation of Nb–O–P heterolinkages.

Figure 12 shows the comparison between RESPDOR ^{31}P spectra acquired with (S) and without (S_0) the application of

the dipolar recoupling scheme on the ^{93}Nb channel. We have selected the spectra for two different evolution times: 4 rotor cycles ($200\ \mu\text{s}$) (Figure 12a,c) and 8 rotor cycles ($400\ \mu\text{s}$) (Figure 12b,d). The difference spectra ($\Delta S = S_0 - S$) are also displayed (dashed curves). The comparison between the RESPDOR S and S_0 spectra reveals that there is an overall dephasing of the spectra, meaning that all ^{31}P species are, to some extent, dipolarly coupled to ^{93}Nb . This reveals the homogeneous NbO_6 units' distribution in the phosphate network. The ΔS curves are slightly shifted to higher chemical shift values, indicating that the replacement of a P–O–P for a P–O–Nb linkage shifts the ^{31}P resonance to a lower field. This observation agrees with our above assignments.

Figure 13 shows the ^{19}F MAS NMR spectra for the investigated glasses. The spectral features are highly dependent on the alkaline earth metal and the concentration of Nb_2O_5 . Specifically, the resonance of fluorine coordinated with phosphorus, P–F (located around $-75\ \text{ppm}$),⁶⁴ is quite pronounced in samples containing between 5 and 15 mol % of Nb_2O_5 . The $^{31}\text{P}\{^{19}\text{F}\}$ -REDOR technique could provide crucial insights for assigning the P–F bond to its specific tetrahedral $[\text{PO}_x\text{F}_{4-x}]$ unit. However, the required probe for this experiment is not currently available in our facilities, and the experiment will be performed soon. For all systems, as the

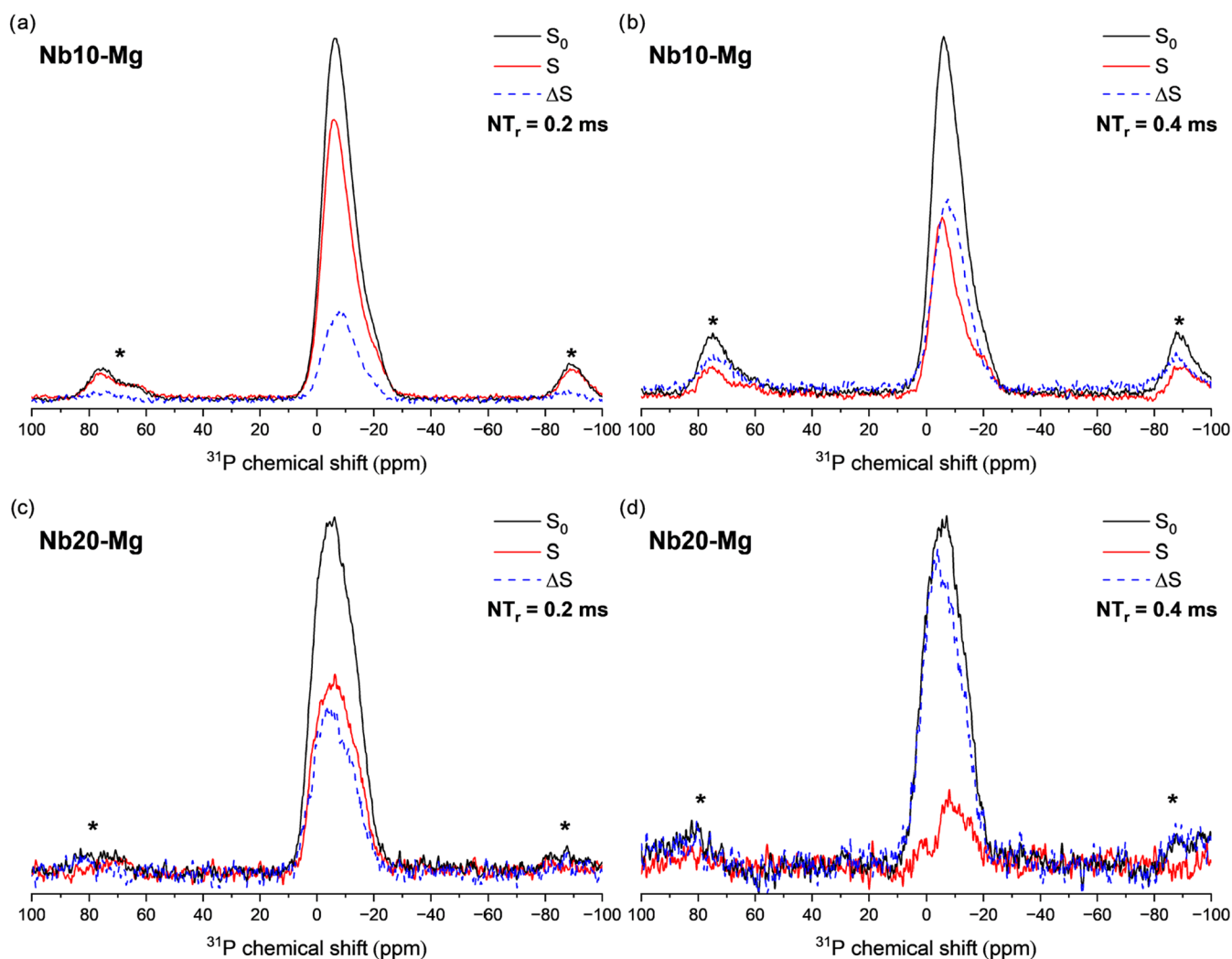


Figure 12. $^{31}\text{P}\{^{93}\text{Nb}\}$ RESPDOR results obtained for Nb10–Mg (a, b) and Nb20–Mg (c, d) glass samples, depicting the S_0 (black curve), S (red curve) and $\Delta S = S_0 - S$ (dashed blue curve) for four rotor cycles (200 μs) (a, c) and eight rotor cycles (400 μs) (b, d).

concentration of Nb_2O_5 increases, the relative intensity of these peaks decreases, indicating that the formation of P–F bonds becomes less probable when compared to the F coordination with Nb and alkaline earth species. In contrast, peaks located between -25 and -40 ppm, and between -120 and -135 ppm, become more prominent with higher concentrations of Nb_2O_5 , particularly in samples with 20 mol % Nb_2O_5 . These peaks are attributed to Nb–F bonds, indicating that the increase of Nb_2O_5 concentration noticeably increases the fluorine coordination with niobium.^{55,65} This trend highlights how the incorporation of Nb_2O_5 influences the bonding environment of fluorine within the glass matrix, altering both the structural and optical properties of the material.⁶⁵

In their study of ^{19}F NMR in various oxyfluoride compounds, Du et al. observed that the displacement of resonances related to Nb–F bonds varies significantly. These variations are influenced not only by the central metal (niobium, in the case of this study) and the cations surrounding the Nb–O–Nb chains, and the presence of other fluorides coordinated to the same Nb atom.⁶⁵ The broad width of the Nb–F bands can be attributed to the unresolved quadrupolar coupling of the neighboring ^{93}Nb nuclei and the positioning of the fluorine nuclei either above or below the

Nb–O–Nb chains.⁶⁵ The Nb5–Ba sample was the only one to exhibit a very narrow and intense peak at approximately -223 ppm, likely indicating the formation of the Na–F bond.⁶⁶ The appearance of this peak at approximately -223 ppm in the Nb5–Ba sample is associated with the high hygroscopic character of this sample, suggesting that crystallization induced by the absorption of atmospheric water led to the formation of Na–F bonds. Regarding the fluorine coordination with different alkaline earth metals, the periodic variation in the ionic radii of each metal and their cationic potential also determines how these bonds are formed within the glass. For instance, the Ba–F bond (expected at -14 ppm) was not detected for any of the Nby–Ba samples. While the Sr–F bond (-85 ppm) was found only for the composition containing 5 mol % of Nb_2O_5 , the Ca–F bond (-107 ppm) was found in the 5, 10, and 15 mol % Nb_2O_5 samples.⁶⁷ Exceptionally, Nby–Mg samples not only clearly showed a Mg–F bond (-192 ppm) for all of the Nby–Mg glasses but also exhibited this peak as the strongest among all fluorine coordination. Therefore, the variable cationic potential between different alkaline earth metals also plays a key role in the coordination with fluorine within the glass and, consequently, rules how the fluorine will be able to coordinate with other species.⁶⁷

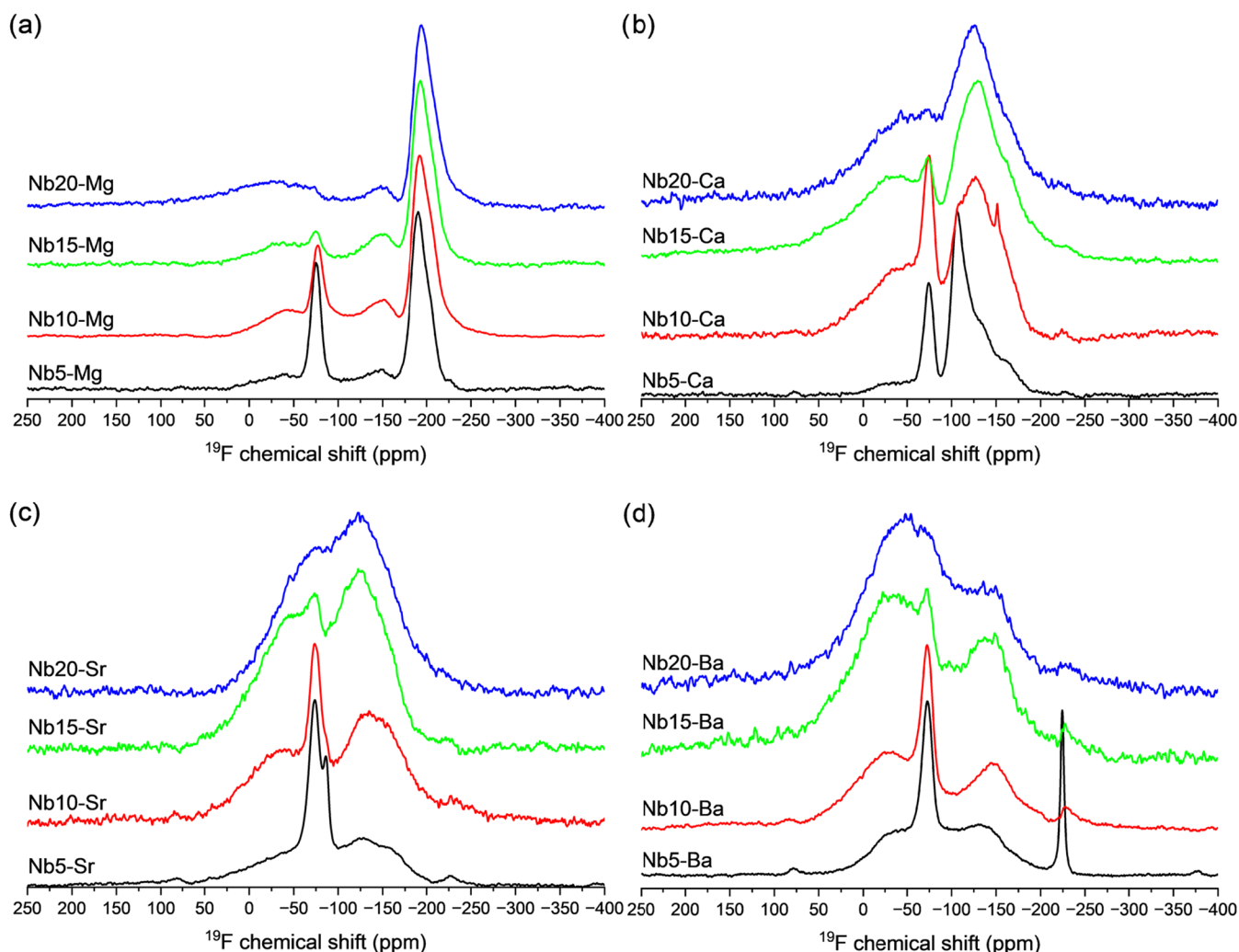


Figure 13. Set of nuclear magnetic resonance (NMR) spectra, monitoring the ^{19}F of Nby-X samples, rotated at 35 kHz, with X = (a) Mg^{2+} , (b) Ca^{2+} , (c) Sr^{2+} , and (d) Ba^{2+} .

The ^{19}F NMR results indicate that fluorine coordination exhibits more pronounced changes compared to that of the ^{31}P nucleus, which is influenced by both the niobium concentration and the type of alkaline earth metal. For instance, the high hygroscopicity of the Nb5-Ba sample resulted in crystallization and the formation of Na-F bonds. This was also detected by ^{23}Na NMR and confirms the earlier assumption that interaction with atmospheric moisture leads to the development of more crystalline domains. Furthermore, the data support the hypothesis that fluorine preferentially coordinates with niobium at higher Nb_2O_5 concentrations, as evidenced by the increased intensity of Nb-F signals with rising niobium content. The results also reinforce the notion that fluorine exhibits a greater affinity for metals with smaller ionic radii. This is demonstrated by the absence of Ba-F bonds, the increasing presence of Sr-F and Ca-F bonds, and the particularly intense Mg-F signal, which remains strong regardless of the Nb_2O_5 concentration. This behavior indicates that fluorine preferentially coordinates with smaller cations, such as magnesium.

Finally, ^{25}Mg MAS NMR spectra were acquired for samples Nb5-Mg and Nb20-Mg (Figure 14). The ^{25}Mg spectral lineshapes are dominated by the quadrupolar coupling interaction and are characterized by a broad distribution of

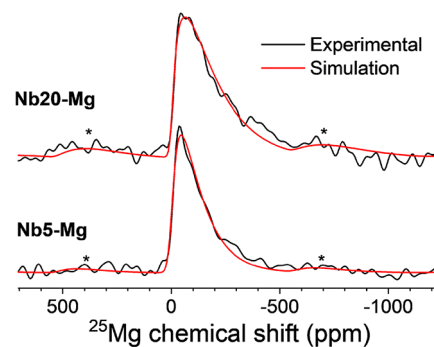


Figure 14. Experimental and simulated ^{25}Mg spectra for Nb5-Mg and Nb20-Mg glass samples. The simulations were performed using an Extended Cjzek model, as described in the main text.

electric field gradients at Mg coordination environments, as typically found for ^{25}Mg NMR in glasses.^{68–75} The lineshapes for both samples could be simulated by using a Cjzek model, which considers a multivariate normal distribution of quadrupolar coupling tensor parameters C_Q and η around an isotropic tensor.⁷⁶ The Cjzek model is characterized by the parameter σ , which corresponds to the standard deviation of the EFG distribution.^{76,77} Both spectra were fitted with a single

Czjzek component, yielding the following parameters: Nb5–Mg: $\delta_{\text{iso}} = 1.7$ ppm, $\sigma = 2.3$ MHz; Nb20–Mg: $\delta_{\text{iso}} = -1.4$ ppm, $\sigma = 3.5$ MHz. It is noteworthy that the isotropic chemical shifts and the Czjzek distribution widths (σ) reported here are significantly smaller than those commonly observed in oxide glasses,^{78–80} which may indeed be a consequence of the stronger and more ordered Mg–F interactions in this fluoride-rich glass matrix. The larger σ value for Nb20–Mg suggests that Nb incorporation leads to a broader EFG distribution at Mg sites, possibly due to increased structural disorder in Mg coordination environments or the presence of multiple distinct Mg sites with varying local structures, which cannot be resolved in the ^{25}Mg spectra. These scenarios cannot be easily distinguished, as both would contribute to line broadening in ^{25}Mg NMR.

4. CONCLUSIONS

A new niobium-fluorophosphate glass matrix was synthesized via a conventional melt-quenching method. A comprehensive investigation was carried out by systematically varying both the Nb_2O_5 content (5, 10, 15, and 20%) and the type of alkaline earth metal (Mg^{2+} , Ca^{2+} , Sr^{2+} , and Ba^{2+}), introduced as their corresponding fluorides. As the Nb_2O_5 content increases, the glass structure evolves due to the progressive substitution of P–O–Nb bonds by Nb–O–Nb linkages, which have a higher degree of covalency and stronger chemical bonding. This structural transformation manifests through several effects: an increase in glass transition temperature (T_g), an alteration of the phosphate units, and a red shift in the ultraviolet absorption edge, corresponding to a reduction in the optical bandgap. Refocused INADEQUATE ^{31}P NMR spectroscopy was employed to monitor the evolution of P^n phosphate units with an increasing niobium content. The addition of Nb_2O_5 leads to alteration of phosphate groups, promotes matrix interconnectivity through the formation of $\text{P}_{1\text{Nb}}^n$, and increases the population of $\text{P}_{2\text{Nb}}^n$ species.

The type of alkaline earth metal also significantly influenced the glass properties. T_g varied primarily as a function of Nb_2O_5 content; however, the crystallization temperatures (T_x and T_p) and the thermal stability parameter (ΔT) were more strongly affected by the identity of the alkaline earth metal. Notably, Ca^{2+} containing glasses exhibited the highest T_x , T_p , and ΔT , with ΔT reaching nearly 400 °C for the Nb10–Ca composition, whereas Ba^{2+} -containing glasses showed no detectable crystallization peaks.

Raman spectroscopy revealed that smaller alkaline earth cations promoted clustering of NbO_6 octahedra, while larger cations induced the elongation of P–O and Nb–O bonds. Furthermore, ^{19}F and ^{25}Mg NMR measurements demonstrated a strong dependence of fluorine coordination on the ionic radius of the alkaline earth metal. F–Mg coordination was consistently intense across all Nb_2O_5 concentrations, while F–Ba interactions were not detected in any of the Nby–Ba samples. These findings help explain the distinct thermal and optical behaviors observed, such as the variations in T_g and optical bandgap energies.

Although Mg^{2+} has a smaller ionic radius and a higher cationic field strength ($Z/r = 2.78 \text{ \AA}^{-1}$), which strengthens the glass network connectivity and increases the glass transition temperature (T_g), its strong affinity for fluoride ions reduces the availability of F^- to stabilize the phosphate chains. At the same time, Mg^{2+} promotes the clustering of NbO_6 units, introducing structural heterogeneities that facilitate crystal-

lization and, consequently, reduce the thermal stability against devitrification (ΔT).

Overall, this study provides valuable insights into how varying P/Nb ratios and the nature of the alkaline earth modifier affect the glass structure and its associated properties. The results support the rational design of fluorophosphonobate glasses with tailored properties for advanced applications, particularly those requiring enhanced chemical and thermal stability.

■ ASSOCIATED CONTENT

Data Availability Statement

All data related to this study are contained within the article and the Supporting Information. Data are available upon request.

Supporting Information

The Supporting Information is available free of charge at <https://pubs.acs.org/doi/10.1021/acsomega.5c05892>.

Photograph of all of the synthesized glass bulks (Figure S1); photograph of the glass bulks containing 5 mol % of Nb_2O_5 after exposure to environmental atmosphere (Figure S2); DSC thermograms related to all synthesized glasses (Figure S3); glass transition temperature of all glasses in the function of the alkaline earth metals' ionic radii (Figure S4); UV–vis–NIR absorption spectra related to all glass bulks (Figure S5); Tauc plot used to calculate Urbach energy, direct and indirect optical bandgap energy values, exemplified for the sample Nb10–Mg (Figure S6); Raman spectra related to all glass bulks (Figure S7); ^{31}P NMR spectra for all glasses (Figure S8); a comparison between ^{31}P single-pulse excitation and INAD experiments for samples Nb5–Mg and Nb20–Mg and the deconvolution of ^{31}P single-pulse excitation for Nb5–Mg spectrum (Figure S9); stacked Raman spectra for the Nby–Ca sample set (Figure S10); ^{23}Na NMR spectra for all glasses (Figure S11); ^{23}Na NMR overlapping Nby–Mg glasses ($y = 5, 10, 15$, and 20 mol % of Nb_2O_5) and Nb20–X glasses ($X = \text{Mg}, \text{Ca}, \text{Sr}$, and Ba) (Figure S12); $^{23}\text{Na}\{^{31}\text{P}\}$ REDOR dephasing curves related to all glasses, containing the comparison with the crystalline $\text{Na}_2\text{PO}_3\text{F}$ reference and parabolic fits for $\Delta S/S_0 \leq 0.25$ (Figure S13); characteristic temperatures (T_g , T_x , T_p , and ΔT) obtained from the DSC thermograms for all glasses (Table S1); calculated relative areas for each assigned phosphate group for sample Nb5–Mg (Table S2); and experimental second moments, $M_2(\text{Na-P})_{\text{exp}}$, obtained from the parabolic fit of the $^{23}\text{Na}\{^{31}\text{P}\}$ REDOR experiments, along with the calculated number of phosphorus species, N_p , for each glass (Table S3) (PDF)

■ AUTHOR INFORMATION

Corresponding Authors

Marcos de Oliveira Junior – São Carlos Institute of Physics (IFSC), University of São Paulo (USP), São Carlos, SP 13566-590, Brazil; orcid.org/0000-0001-6538-2204; Email: mjunior@ifsc.usp.br

Danilo Manzani – São Carlos Institute of Chemistry (IQSC), University of São Paulo (USP), São Carlos, SP 13566-590, Brazil; orcid.org/0000-0001-7280-5404; Email: dmanzani@usp.br

Authors

Leandro Olivetti Estevam da Silva – São Carlos Institute of Chemistry (IQSC), University of São Paulo (USP), São Carlos, SP 13566-590, Brazil; orcid.org/0000-0001-9241-1285

Lais Dantas Silva – Department of Chemistry and Biology, State University of Maranhão (UEMA), Caxias, MA 65604-380, Brazil; orcid.org/0000-0003-2247-0268

Edgar Dutra Zanotto – Center for Research, Technology, and Education in Vitreous Materials (CeRTEV), Department of Materials Engineering (DEMa), Federal University of São Carlos (UFSCar), São Carlos, SP 13565-905, Brazil; orcid.org/0000-0003-4931-4505

Complete contact information is available at:

<https://pubs.acs.org/10.1021/acsomega.5c05892>

Funding

The Article Processing Charge for the publication of this research was funded by the Coordenação de Aperfeiçoamento de Pessoal de Nível Superior (CAPES), Brazil (ROR identifier: 00x0ma614).

Notes

The authors declare no competing financial interest.

ACKNOWLEDGMENTS

The authors acknowledge grants from São Paulo Research Foundation (FAPESP) (Project Nos. 2013/07793-6, 2019/16115-8, 2021/08111-2, 2022/01762-0, 2023/05994-6, 2023/09794-1, and 2024/17334-3) and Conselho Nacional de Desenvolvimento Científico e Tecnológico (CNPq) (Project Nos. 405048/2021-1, 440225/2021-3, 312802/2023-4, and 304718/2023-08) for financial support. AI-based language models (DeepL and Google Gemini) were used to revise and improve writing. All suggested changes were carefully reviewed, validated, and approved by the authors before submitting the manuscript.

REFERENCES

- (1) Ehrt, D. Phosphate and fluoride phosphate optical glasses—properties, structure and applications. *Phys. Chem. Glasses: Eur. J. Glass Sci. Technol., Part B* **2015**, *56* (6), 217–234.
- (2) Fazal, S.; Zaman, F.; Ali, S.; Iqbal, Y.; Chanithima, N.; Tuscharoen, S.; Ali, M.; Hayat, K.; Zulfiqar, S.; Arshad, M.; El-Denglawey, A.; Kaewkhao, J. Investigation of europium-doped aluminium phosphate glass for red light generation. *Ceram. Int.* **2022**, *48* (17), 24751–24757.
- (3) Farag, M. A.; Ibrahim, A.; Hassaan, M. Y.; Ramadan, R. M. Enhancement of structural and optical properties of transparent sodium zinc phosphate glass—ceramics nano composite. *J. Aust. Ceram. Soc.* **2022**, *58* (2), 653–661.
- (4) Möncke, D.; Eckert, H. Review on the structural analysis of fluoride-phosphate and fluoro-phosphate glasses. *J. Non-Cryst. Solids: X* **2019**, *3*, No. 100026.
- (5) Wang, X.; Tian, Y.; Zhang, Y.; Tang, D.; Li, B.; Zhang, J.; Xu, S. Effect of $\text{Al}(\text{PO}_3)_3$, NaF, and SrF_2 on structure and properties of fluorophosphate glass. *J. Non-Cryst. Solids* **2023**, *602*, No. 122089.
- (6) Sallam, O. I.; Atta, M. M.; Taha, E. O.; Elbasiony, A. M.; Henaish, A. M. A.; Ahmed, R. M. Synthesis and modification of photoluminescence and dielectric properties of novel fluorophosphate glass by incorporating different transition metal oxides for optoelectronic applications. *Opt. Mater.* **2023**, *136*, No. 113413.
- (7) Möncke, D.; da Cruz Barbosa Neto, M.; Bradtmüller, H.; de Souza, G. B.; Rodrigues, A. M.; Elkholy, H. S.; Othman, H. A.; Moulton, B. J. A.; Kamitsos, E. I.; Rodrigues, A. C. M.; Ehrt, D. $\text{NaPO}_3\text{-AlF}_3$ glasses: fluorine evaporation during melting and the resulting variations in structure and properties. *J. Chem. Technol. Metall.* **2018**, *53* (6), 1047–1060.
- (8) Cao, X.; Wang, P.; Wan, R.; Guo, C.; Tian, S. Structural insight of fluorophosphate glasses through F/O ratio: Case study of Raman and NMR spectra. *J. Non-Cryst. Solids* **2024**, *637*, No. 123065.
- (9) Iturraran, N.; Huraux, K.; Bao, Y.; Gawne, D. T.; Guilment, J. Effect of melting parameters during synthesis on the structure and properties of tin fluoride phosphate glasses. *J. Non-Cryst. Solids* **2018**, *489*, 64–70.
- (10) de Oliveira, M., Jr.; Gonçalves, T. S.; Ferrari, C.; Magon, C. J.; Pizani, P. S.; de Camargo, A. S. S.; Eckert, H. Structure–property relations in fluorophosphate glasses: An integrated spectroscopic strategy. *J. Phys. Chem. C* **2017**, *121* (5), 2968–2986.
- (11) Capelo, R. G.; Gerdes, J. M.; Rehfuß, U.; Silva, L. D.; Hansen, M. R.; van Wüllen, L.; Eckert, H.; Manzani, D. Structural characterization of a new fluorophosphotellurite glass system. *Dalton Trans.* **2023**, *52* (8), 2227–2242.
- (12) Teixeira, Z.; Alves, O. L.; Mazali, I. O. Structure, thermal behavior, chemical durability, and optical properties of the $\text{Na}_2\text{O-Al}_2\text{O}_3\text{-TiO}_2\text{-Nb}_2\text{O}_5\text{-P}_2\text{O}_5$ glass system. *J. Am. Ceram. Soc.* **2007**, *90* (1), 256–263.
- (13) Manzani, D.; Gualberto, T.; Almeida, J. M.; Montesso, M.; Mendonça, C. R.; Rivera, A.; De Boni, L.; Nalin, M.; Ribeiro, S. J. Highly nonlinear $\text{Pb}_2\text{P}_2\text{O}_7\text{-Nb}_2\text{O}_5$ glasses for optical fiber production. *J. Non-Cryst. Solids* **2016**, *443*, 82–90.
- (14) Campos, G. O.; Clabel, H. J.; Pelosi, A. G.; Pelosi, A. G.; da Silva, L. O. E.; da Silva, L. O. E.; Mastelaro, V. R.; Mastelaro, V. R.; Manzani, D.; Manzani, D.; Mendonça, C. R. Effect of WO_3 in the third-order optical nonlinearities of tungsten lead pyrophosphate glasses. *Opt. Mater.* **2024**, *150*, No. 115278.
- (15) Alves, A. R.; Coutinho, A. D. R. The evolution of the niobium production in Brazil. *Mater. Res.* **2015**, *18* (1), 106–112.
- (16) Varshneya, A. K.; Mauro, J. C. Glass Compositions and Structures. In *Fundamentals of Inorganic Glasses*, 3rd ed.; Varshneya, A. K.; Mauro, J. C., Eds.; Elsevier: Oxford, U.K., 2019; pp 101–163.
- (17) Topper, B.; Greiner, L.; Youngman, R. E.; Stohr, D.; Kamitsos, E. I.; Möncke, D. Effect of modifier cation size on the structure, properties and nickel speciation in BK7 type alkali borosilicate glasses. *J. Non-Cryst. Solids: X* **2023**, *17*, No. 100161.
- (18) Poojha, M. K.; Naseer, K. A.; Matheswaran, P.; Marimuthu, K.; El Shiekh, E. Effect of alkali/alkaline modifiers on Pr^{3+} ions doped lead boro-tellurite glasses for lasing material applications. *Opt. Mater.* **2023**, *143*, No. 114289.
- (19) Guedes, L. F. N.; Marcondes, L. M.; Evangelista, R. O.; Batista, G.; Mendoza, V. G.; Cassanjes, F. C.; Poirier, G. Y. Effect of alkaline modifiers on the structural, optical and crystallization properties of niobium germanate glasses and glass-ceramics. *Opt. Mater.* **2020**, *105*, No. 109866.
- (20) Mercier, C.; Palavit, G.; Montagne, L.; Follet-Houttemane, C. A survey of transition-metal-containing phosphate glasses. *C. R. Chim.* **2002**, *5* (11), 693–703.
- (21) Griebenow, K.; Bragatto, C. B.; Kamitsos, E. I.; Wondraczek, L. Mixed-modifier effect in alkaline earth metaphosphate glasses. *J. Non-Cryst. Solids* **2018**, *481*, 447–456.
- (22) Cory, D. G.; Ritchey, W. M. Suppression of signals from the probe in Bloch decay spectra. *J. Magn. Reson. (1969)* **1988**, *80* (1), 128–132.
- (23) Guerry, P.; Smith, M. E.; Brown, S. P. ^{31}P MAS refocused INADEQUATE spin-echo (REINE) NMR spectroscopy: revealing J coupling and chemical shift two-dimensional correlations in disordered solids. *J. Am. Chem. Soc.* **2009**, *131* (33), 11861–11874.
- (24) Bertmer, M.; Eckert, H. Dephasing of spin echoes by multiple heteronuclear dipolar interactions in rotational echo double resonance NMR experiments. *Solid State Nucl. Magn. Reson.* **1999**, *15* (3), 139–152.
- (25) Gullion, T. Measurement of dipolar interactions between spin-1/2 and quadrupolar nuclei by rotational-echo, adiabatic-passage, double-resonance NMR. *Chem. Phys. Lett.* **1995**, *246* (3), 325–330.

- (26) Wübker, A.; Koppe, J.; Bradtmüller, H.; Keweloh, L.; Pleschka, D.; Uhl, W.; Hansen, M. R.; Eckert, H. Solid-State Nuclear Magnetic Resonance Techniques for the Structural Characterization of Geminal Alane-Phosphate Frustrated Lewis Pairs and Secondary Adducts. *Chem.—Eur. J.* **2021**, *27* (52), 13249–13257.
- (27) O'Dell, L. A. The WURST kind of pulses in solid-state NMR. *Solid State Nucl. Magn. Reson.* **2013**, *55–56*, 28–41.
- (28) Bak, M.; Rasmussen, J. T.; Nielsen, N. C. SIMPSON: a general simulation program for solid-state NMR spectroscopy. *J. Magn. Reson.* **2011**, *213* (2), 366–400.
- (29) Bradtmüller, H.; Zheng, Q.; Gaddam, A.; et al. Structural impact of niobium oxide on lithium silicate glasses: Results from advanced interaction-selective solid-state nuclear magnetic resonance and Raman spectroscopy. *Acta Mater.* **2023**, *255*, No. 119061.
- (30) Yao, Z.; Kwak, H. T.; Sakellariou, D.; Emsley, L.; Grandinetti, P. J. Sensitivity enhancement of the central transition NMR signal of quadrupolar nuclei under magic-angle spinning. *Chem. Phys. Lett.* **2000**, *327* (1–2), 85–90.
- (31) Dey, K. K.; Prasad, S.; Ash, J. T.; Deschamps, M.; Grandinetti, P. J. Spectral editing in solid-state MAS NMR of quadrupolar nuclei using selective satellite inversion. *J. Magn. Reson.* **2007**, *185* (2), 326–330.
- (32) Freitas, J. C. C.; Wong, A.; Smith, M. E. Solid-state natural abundance ^{25}Mg NMR studies of $\text{Na}_2\text{MgEDTA} \cdot 4\text{H}_2\text{O}$ —a possible new reference compound for ^{25}Mg NMR spectroscopy. *Magn. Reson. Chem.* **2009**, *47* (1), 9–15.
- (33) Freitas, J. C.; Smith, M. E. Recent Advances in Solid-State ^{25}Mg NMR Spectroscopy. *Annual Reports on NMR Spectroscopy*; Elsevier B.V., 2012; Vol. 75, pp 25–114.
- (34) Sreenivasan, H.; Kinnunen, P.; Adesanya, E.; Patanen, M.; Kantola, A. M.; Telkki, V. V.; Huttula, M.; Cao, W.; Provis, J. L.; Illikainen, M. Field strength of network-modifying cation dictates the structure of (Na-Mg) aluminosilicate glasses. *Front. Mater.* **2020**, *7*, No. 267.
- (35) Petrovskii, G. T.; Golubkov, V. V.; Dymshits, O. S.; Zhilin, A. A.; Shepilov, M. P. Phase Separation and Crystallization in Glasses of the Na_2O – K_2O – Nb_2O_5 – SiO_2 System. *Glass Phys. Chem.* **2003**, *29*, 243–253.
- (36) Mošner, P.; Hostinský, T.; Koudelka, L. Thermal, structural and crystallization study of Na_2O – P_2O_5 – Nb_2O_5 glasses. *J. Solid State Chem.* **2022**, *316*, No. 123545.
- (37) Shannon, R. D. Revised effective ionic radii and systematic studies of interatomic distances in halides and chalcogenides. *Acta Crystallogr., Sect. A* **1976**, *32*, 751–767.
- (38) Ciceo, R. L.; Todea, M.; Toloman, D.; Muresan-Pop, M.; Simon, V. Structure-composition correlation in niobium containing borophosphate glasses. *J. Non-Cryst. Solids* **2020**, *542*, No. 120102.
- (39) Cicconi, M. R.; Kimura, K.; Bradtmüller, H.; Deng, H.; Kohara, S.; Onodera, Y.; Hayakawa, T.; Shimono, S.; Hayashi, K.; de Ligny, D. Unraveling the structural complexity of niobate units in aluminosilicate glasses and glass–ceramics. *Mater. Adv.* **2025**, *6* (12), 3863–3874.
- (40) Koudelka, L.; Pospíšil, J.; Mošner, P.; Montagne, L.; Delevoye, L. Structure and properties of potassium niobato-borophosphate glasses. *J. Non-Cryst. Solids* **2008**, *354* (2–9), 129–133.
- (41) Orel, B.; Maček, M.; Grdadolnik, J.; Meden, A. In situ UV-Vis and ex situ IR spectroelectrochemical investigations of amorphous and crystalline electrochromic Nb_2O_5 films in charged/discharged states. *J. Solid State Electrochem.* **1998**, *2*, 221–236.
- (42) Louzguine, D. V.; Inoue, A. Electronegativity of the constituent rare-earth metals as a factor stabilizing the supercooled liquid region in Al-based metallic glasses. *Appl. Phys. Lett.* **2001**, *79* (21), 3410–3412.
- (43) Stunda-Zujeva, A.; Vecstaudža, J.; Kriekš, G.; Bērziņa-Cimdiņa, L. Glass Formation and Crystallization in P_2O_5 – Nb_2O_5 – CaO – Na_2O System. *Mater. Sci. Appl. Chem.* **2017**, *34* (1), 21–28.
- (44) Ledemi, Y.; Trudel, A. A.; Rivera, V. A.; Chenu, S.; Véron, E.; Nunes, L. A.; Allix, M.; Messaddeq, Y. White light and multicolor emission tuning in triply doped $\text{Yb}^{3+}/\text{Tm}^{3+}/\text{Er}^{3+}$ novel fluoro-phosphate transparent glass-ceramics. *J. Mater. Chem. C* **2014**, *2* (25), 5046–5056.
- (45) Duffy, J. A. Optical basicity: a practical acid-base theory for oxides and oxyanions. *J. Chem. Educ.* **1996**, *73* (12), 1138–1142.
- (46) Marzouk, S. Y.; Seoudi, R.; Said, D. A.; Mabrouk, M. S. Linear and non-linear optics and FTIR characteristics of borosilicate glasses doped with gadolinium ions. *Opt. Mater.* **2013**, *35* (12), 2077–2084.
- (47) Hammad, A. H.; Abdelghany, A. M. Optical and structural investigations of zinc phosphate glasses containing vanadium ions. *J. Non-Cryst. Solids* **2016**, *433*, 14–19.
- (48) Yakuphanoglu, F.; Arslan, M. The fundamental absorption edge and optical constants of some charge transfer compounds. *Opt. Mater.* **2004**, *27* (1), 29–37.
- (49) Rivera, V. A. G.; Ledemi, Y.; Pereira-da-Silva, M. A.; Messaddeq, Y.; Marega, E., Jr. Plasmon-photon conversion to near-infrared emission from Yb^{3+} :(Au/Ag-nanoparticles) in tungsten-tellurite glasses. *Sci. Rep.* **2016**, *6* (1), No. 18464.
- (50) Nageno, Y.; Takebe, H.; Morinaga, K.; Izumitani, T. Effect of modifier ions on fluorescence and absorption of Eu^{3+} in alkali and alkaline earth silicate glasses. *J. Non-Cryst. Solids* **1994**, *169* (3), 288–294.
- (51) Qteish, A. Electronegativity scales and electronegativity-bond ionicity relations: a comparative study. *J. Phys. Chem. Solids* **2019**, *124*, 186–191.
- (52) Chenu, S.; Werner-Zwanziger, U.; Calahoo, C.; Zwanziger, J. W. Structure and properties of NaPO_3 – ZnO – Nb_2O_5 – Al_2O_3 glasses. *J. Non-Cryst. Solids* **2012**, *358* (15), 1795–1805.
- (53) El Jazouli, A.; Parent, C.; Dance, J. M.; Le Flem, G.; Hagenmuller, P.; Viala, J. C. $\text{Na}_4\text{Nb}(\text{PO}_4)_3$, a material with a reversible crystal-glass transformation: structural and optical comparison. *J. Solid State Chem.* **1988**, *74* (2), 377–384.
- (54) Flambard, A.; Videau, J. J.; Delevoye, L.; Cardinal, T.; Labrugère, C.; Rivero, C. A.; Couzi, M.; Montagne, L. Structure and nonlinear optical properties of sodium–niobium phosphate glasses. *J. Non-Cryst. Solids* **2008**, *354* (30), 3540–3547.
- (55) da Silva, L. O. E.; Rivera, V. A. G.; Falci, R.; Messaddeq, Y.; de Oliveira Junior, M.; Manzani, D. Fluorine alkaline earth (MgF_2 , CaF_2 , SrF_2 , BaF_2) influence on thermal, structural, and luminescent properties of Eu^{3+} -doped niobium phospho-fluoride glass. *Mater. Res. Bull.* **2025**, *185*, No. 113291.
- (56) Faleiro, J. H.; Dantas, N. O.; Silva, A. C.; Barbosa, H. P.; Da Silva, B. H.; Lima, K. D. O.; Silva, G. F.; Gonçalves, R. R.; Falci, R.; Massadeq, Y.; Branco, I. D. O.; Cerrutti, B. M.; Bradtmüller, H.; Eckert, H.; Ferrari, J. L. Niobium incorporation into rare-earth doped aluminophosphate glasses: Structural characterization, optical properties, and luminescence. *J. Non-Cryst. Solids* **2023**, *605*, No. 122173.
- (57) Musgraves, J. D.; Hu, J.; Calvez, L. Glass Families. In *Springer Handbook of Glass*; Musgraves, J. D.; Hu, J.; Calvez, L., Eds.; Springer Nature: Cham, Switzerland, 2019; pp 441–842.
- (58) Kirkpatrick, R. J.; Brow, R. K. Nuclear magnetic resonance investigation of the structures of phosphate and phosphate-containing glasses: a review. *Solid State Nucl. Magn. Reson.* **1995**, *5* (1), 9–21.
- (59) Arunkumar, S.; Krishnaiah, K. V.; Marimuthu, K. Structural and luminescence behavior of lead fluoroborate glasses containing Eu^{3+} ions. *Phys. B* **2013**, *416*, 88–100.
- (60) Muñoz-Senovilla, L.; Muñoz, F. Behaviour of viscosity in metaphosphate glasses. *J. Non-Cryst. Solids* **2014**, *385*, 9–16.
- (61) Sene, F. F.; Martinelli, J. R.; Gomes, L. Optical and structural characterization of rare earth doped niobium phosphate glasses. *J. Non-Cryst. Solids* **2004**, *348*, 63–71.
- (62) Bertmer, M.; Züchner, L.; Chan, J. C.; Eckert, H. Short and medium range order in sodium aluminoborate glasses. 2. Site connectivities and cation distributions studied by rotational echo double resonance NMR spectroscopy. *J. Phys. Chem. B* **2000**, *104* (28), 6541–6553.
- (63) Van Vleck, J. H. The dipolar broadening of magnetic resonance lines in crystals. *Phys. Rev.* **1948**, *74* (9), 1168–1183.
- (64) Bradtmüller, H.; Zhang, L.; De Araujo, C. C.; Eckert, H.; Möncke, D.; Ehart, D. Structural studies of NaPO_3 – AlF_3 glasses by

high-resolution double-resonance nuclear magnetic resonance spectroscopy. *J. Phys. Chem. C* **2018**, 122 (37), 21579–21588.

(65) Du, L. S.; Wang, F.; Grey, C. P. High-Resolution ^{19}F MAS and ^{19}F – ^{113}Cd REDOR NMR study of oxygen/fluorine ordering in oxyfluorides. *J. Solid State Chem.* **1998**, 140 (2), 285–294.

(66) Stebbins, J. F.; Zeng, Q. Cation ordering at fluoride sites in silicate glasses: a high-resolution ^{19}F NMR study. *J. Non-Cryst. Solids* **2000**, 262 (1–3), 1–5.

(67) Sadoc, A.; Body, M.; Legein, C.; Biswal, M.; Fayon, F.; Rocquefelte, X.; Boucher, F. NMR parameters in alkali, alkaline earth and rare earth fluorides from first principle calculations. *Phys. Chem. Chem. Phys.* **2011**, 13 (41), 18539–18550.

(68) Shimoda, K.; Tobu, Y.; Hatakeyama, M.; Nemoto, T.; Saito, K. Structural investigation of Mg local environments in silicate glasses by ultra-high field ^{25}Mg 3QMAS NMR spectroscopy. *Am. Mineral.* **2007**, 92 (4), 695–698.

(69) Shimoda, K.; Okuno, M. Molecular dynamics study of CaSiO_3 – MgSiO_3 glasses under high pressure. *J. Phys.: Condens. Matter* **2006**, 18 (28), 6531–6544.

(70) Shimoda, K.; Nemoto, T.; Saito, K. Local structure of magnesium in silicate glasses: a ^{25}Mg 3QMAS NMR study. *J. Phys. Chem. B* **2008**, 112 (22), 6747–6752.

(71) Backhouse, D. J.; Corkhill, C. L.; Hyatt, N. C.; Hand, R. J. Investigation of the role of Mg and Ca in the structure and durability of aluminoborosilicate glass. *J. Non-Cryst. Solids* **2019**, 512, 41–52.

(72) Bisbrouck, N.; Bertani, M.; Angeli, F.; Charpentier, T.; de Ligny, D.; Delaye, J. M.; Gin, S.; Micoulaut, M. Impact of magnesium on the structure of aluminoborosilicate glasses: A solid-state NMR and Raman spectroscopy study. *J. Am. Ceram. Soc.* **2021**, 104 (9), 4518–4536.

(73) Cormier, L.; Cuello, G. J. Structural investigation of glasses along the MgSiO_3 – CaSiO_3 join: Diffraction studies. *Geochim. Cosmochim. Acta* **2013**, 122, 498–510.

(74) Watts, S. J.; Hill, R. G.; O'Donnell, M. D.; Law, R. V. Influence of magnesia on the structure and properties of bioactive glasses. *J. Non-Cryst. Solids* **2010**, 356 (9–10), 517–524.

(75) Kroeker, S.; Stebbins, J. F. Magnesium coordination environments in glasses and minerals: New insight from high-field magnesium-25 MAS NMR. *Am. Mineral.* **2000**, 85 (10), 1459–1464.

(76) Czjzek, G.; Fink, J.; Götz, F.; Schmidt, H.; Coey, J. M. D.; Rebouillat, J. P.; Liénard, A. Atomic coordination and the distribution of electric field gradients in amorphous solids. *Phys. Rev. B* **1981**, 23 (6), 2513–2530.

(77) Van Meerten, S. G. J.; Franssen, W. M. J.; Kentgens, A. P. M. ssNake: A cross-platform open-source NMR data processing and fitting application. *J. Magn. Reson.* **2019**, 301, 56–66.

(78) Mohammadi, H.; Mendes Da Silva, R.; Zeidler, A.; Gammond, L. V.; Gehlhaar, F.; de Oliveira, M.; Damasceno, H.; Eckert, H.; Youngman, R. E.; Aitken, B. G.; Fischer, H. E.; Kohlmann, H.; Cormier, L.; Benmore, C. J.; Salmon, P. S. Structure of diopside, enstatite, and magnesium aluminosilicate glasses: A joint approach using neutron and x-ray diffraction and solid-state NMR. *J. Chem. Phys.* **2022**, 157 (21), No. 214503.

(79) de Oliveira, M., Jr.; Damasceno, H.; Salmon, P. S.; Eckert, H. Analysis and information content of quadrupolar NMR in glasses: ^{25}Mg NMR in vitreous MgSiO_3 and $\text{CaMgSi}_2\text{O}_6$. *J. Magn. Reson. Open* **2022**, 12–13, No. 100067.

(80) Sen, S.; Stebbins, J. F.; Kroeker, S.; Hung, I.; Gan, Z. Evidence for Mixed Mg Coordination Environments in Silicate Glasses: Results from ^{25}Mg NMR Spectroscopy at 35.2 T. *J. Phys. Chem. B* **2023**, 127 (49), 10659–10666.



CAS BIOFINDER DISCOVERY PLATFORM™

CAS BIOFINDER HELPS YOU FIND YOUR NEXT BREAKTHROUGH FASTER

Navigate pathways, targets, and
diseases with precision

Explore CAS BioFinder



A Division of the
American Chemical Society